Scientific Reports

https://doi.org/10.1038/s41598-026-42761-z

Article in Press

# Noninvasive hemodynamic assessment of aortic coarctation: multimodal imaging based-computational fluid dynamics

Received: 14 September 2025

Accepted: 27 February 2026

Published online: 09 March 2026

Cite this article as: Hu M., Li X., Wang H. *et al.* Noninvasive hemodynamic assessment of aortic coarctation: multimodal imaging based-computational fluid dynamics. *Sci Rep* (2026). https://doi.org/10.1038/s41598-026-42761-z

Mengsi Hu, Xia Li, Huihui Wang, Yuezhong Zhang, Ximing Wang, Jikai Liu, Zhenxia Mu, Peixian Gao & Xiufeng Song

# Title Page

# Noninvasive Hemodynamic Assessment of Aortic Coarctation: Multimodal imaging Based-Computational Fluid Dynamics

Mengsi Hu, MD;[1, 2#]; Xia Li, MD [3#]; Huihui Wang, MD, [3*]; Yuezhong Zhang, MD [3*]; Ximing Wang MD, PhD [4]; Jikai Liu, PhD [5]; Zhenxia Mu, MD [4]; Peixian Gao, MD [6]; Xiufeng Song, MS [7]

[1]Department of Nephrology, Shandong Provincial Hospital Affiliated to Shandong First Medical University, Jinan, China

[2]Department of Nephrology, Shandong Provincial Hospital, Cheeloo College of Medicine, Shandong University, Jinan, China

[3]Department of Ultrasound, Shandong Provincial Hospital Affiliated to Shandong First Medical University, Jinan, China

[4]Department of Imaging, Shandong Provincial Hospital, Cheeloo College of Medicine, Shandong University, Jinan, China

[5]Key Laboratory of High Efficiency and Clean Mechanical Manufacture (Ministry of Education), School of Mechanical Engineering, Shandong University, Jinan, China

[6]Department of Vascular Surgery, Shandong Provincial Hospital, Cheeloo College of Medicine, Shandong University, Jinan, China

[7]Department of Dermatology, The Third Affiliated Hospital of Shandong First Medical University Affiliated Hospital of Shandong Academy of Medical Sciences, Jinan, China

[#]These authors contributed equally to this manuscript.

[*]Correspondence to: Huihui Wang, MD, Department of Ultrasound, Shandong Provincial Hospital Affiliated to Shandong First Medical University, Jinan,250021, China ; Email: wenddywang@126.com;

*Yuezhong Zhang, MD, Department of Ultrasound, Shandong Provincial Hospital Affiliated to Shandong First Medical University, Jinan, 250021, China; Email: zhangyuezhong@sdfmu.edu.cn

**Short title**: Multimodal imaging Based-CFD assessment of CoA

**Abstract**

The gold standard assessment of coarctation of aorta (CoA) was achieved invasively by cardiac catheterization, which is associated with several risks including radiation exposure. The present study aimed to validate a multimodal imaging-based non-invasive computational framework for assessment of trans-coarctation pressure gradients (PG) in patients with severe coarctation of the aorta (CoA). Here we developed a non-invasive computational fluid dynamics (CFD) modeling framework based on multidetector computed tomography angiography (MDCTA) and ultrasound-derived input parameters, which incorporated into a lumped parameter model (LPM) and validated the results against measurements obtained via cardiac catheterization, both preoperatively and postoperatively. We used conventional Doppler estimates to make these correlations and to compare their diagnostic performance in identifying critical PG. The results indicated that for 18 patients with severe CoA the CFD simulation exhibited better concordance and correlation with catheter measurements compared to Doppler gradients (pre-intervention: 58.44±17.77 vs. 55.72±19.71 vs.57.78±18.02 mmHg; post-intervention: 17.94±10.54 vs. 15.65±5.15 vs.20.61 ± 7.43 mmHg). Specifically, the CFD-derived PG showed a stronger correlation with catheter measurements (pre-intervention r = 0.89, post-intervention r = 0.90) than did Doppler-derived PG (pre-intervention r = 0.71, post-intervention r = 0.30). This CFD framework facilitated reliable quantification of PG and visualization of hemodynamic forces in patient-specific geometric models, and suggesting its potential as a non-invasive and effective approach for the assessment of CoA.

**key words** aorta coarctation, CoA, computational fluid dynamics, MDCTA, Doppler, pressure gradient, PG

## Introduction

Coarctation of aorta (CoA) is characterized by a partial or long-segment narrowing of the descending aorta, typically occurring near or distal to the aortic arch [1], accounting for approximately 5-7% of congenital heart disease cases, affecting 3-4 per 10000 newborns per year[2, 3]. It occurs with a wide spectrum of hemodynamic severity

and clinical manifestations, ranging from asymptomatic mild narrowing to severe obstruction leading to left ventricular (LV) failure [4-6]. CoA leads to increased afterload on the left ventricle, exposure of the upper body to hypertension, flow disturbance in the thoracic aorta, and diminished perfusion to the lower body [7, 8]. If left untreated, CoA is associated with an increased risk of premature coronary artery disease, stroke, endocarditis, aortic dissection and heart failure [9]. Literature indicates that among adults over 40 years of age with uncorrected CoA and severe symptoms, around 60% might develop heart failure, 75% may die by the age of 50, and 90% by age of 60 [10, 11]. Therefore, early diagnosis and intervention are critical for managing the disease and preventing associated complications.

The criterion standard for assessing the severity of coarctation is the measurement of the peak systolic pressure drop across the narrowing, typically achieved through invasive cardiac catheterization [7] [12], However, this invasive method might pose significant risks to patients [13]. Typical non-invasive imaging modalities for diagnosing CoA include echocardiography, multidetector CT angiography (MDCTA) and magnetic resonance imaging (MRI) [14, 15], which offer temporally and spatially resolved information of patient-specific anatomical and functional characteristics, such as flow conditions and vascular deformations [16]. Nevertheless, obtaining accurate hemodynamic measurements derived from Doppler echocardiography can be challenging in older children and adults due to the posterior position of the descending aorta. And studies have reported that Doppler echocardiography may overestimate the pressure gradients, irrespective of whether simplified or modified Bernoulli's equation [17]. MDCTA or CMR alone cannot assess the pressure drop and therefore cannot judge the severity with accuracy [7].

From this point of view, a robust non-invasive assessment of pressure gradients (PGs) could mitigate these limitations and simultaneously reducing overall costs and patient risks associated with both preoperative and postoperative assessment of CoA. In recent years, CFD models have been investigated to analyze hemodynamics in both healthy and diseased aortic geometries, utilizing either idealized and/or patient-specific parameters. These models have demonstrated their ability to predict pressure drop across the coarctation non-invasively, incorporating factors such as rigid [18] or compliant vessel walls [19], oscillatory wall shear stress, and turbulence intensity [20]. Of note, many CFD models from previous studies have relied on parameters derived from invasive measurements. Bonfanti et al introduced a calibration method for

resistance and compliances used in the Windkessel or lumped parameter models (LPM), and compared the pressures at various locations calculated by CFD with invasive measurements [21]. Keshavarz-Motamed et al presented a patient-specific CFD framework that demonstrated strong concordance between the pressure waveforms obtained upstream and downstream of the CoA in simulations and catheter data in a cohort of 34 patients with CoA, reporting a maximum relative error of only 3.8% the peak-to-peak PG [4].

In this study, we developed a multimodal, patient-specific, non-invasive computational framework to assess the PG across CoA. This framework integrated patient-specific geometry from MDCTA with a coupled computational fluid dynamics (CFD) and lumped parameter model (LPM) approach, utilizing boundary conditions derived from Doppler echocardiography and cuff blood pressures (BPs) from the upper and lower extremities. We subsequently validated these findings against invasive catheter measurements and Doppler echocardiography results. Furthermore, we evaluated hemodynamic indices both pre- and post-intervention, including flow velocity, wall pressure distribution, and wall shear stress in patients with CoA.

## Methods

### Study population

A cohort of 18 patients (11 males and 7 females), aged between 6 to 49 years, diagnosed with severe CoA in accordance with the guidelines by the American Heart Association (AHA)/American College of Cardiology (ACC) [22], were enrolled in this retrospective study at Shandong Provincial Hospital Affiliated to Shandong First Medical University from May 2015 to February 2024. The standard CoA diagnostic protocol at our institution included the following: measurement of the BPs with a cuff BP gauge at the upper and lower extremities, acquisition of MDCTA images of the thoracic aorta, and assessment of the CoA by Doppler echocardiography estimates. Inclusion criteria of this study were set as follows: (1) a pressure difference of ≥20mmHg between the upper and lower extremity, as measured by the cuff BP gauge; and (2) confirmation of the PG via Doppler echocardiography and MDCTA imaging, with subsequent cardiac catheterization performed. Exclusion criteria included: (1) the presence of comorbidities such as heart failure with a left ventricular ejection fraction (LVEF) ≤ 40%; (2) a time interval exceeding 2 weeks between preoperative and postoperative assessments via MDCTA, echocardiography, and vascular ultrasound; (3) the presence of patent ductus arteriosus (PDA) and extensive collateral circulation; and (4) conditions such as lower limb arterial thrombosis, thromboangiitis obliterans, multiple arteritis, and other

diseases causing lower limb ischemic symptoms (Supplementary Figure S1).

Patient data were reviewed and extracted from electronic medical records, including symptoms, pre- and post-intervention BPs of upper and lower extremities, PGs obtained from cardiac catheterization, pre-and post-operative creatinine and urea nitrogen, levels and data from echocardiography and vascular ultrasound. Non-invasive BP measurements were conducted three times consecutively with interval time of 1-2 mins using a cuff device before and after the intervention, by placing the cuff device on the upper and lower extremities. The study protocol conforms to the ethical guidelines of the Declaration of Helsinki. The retrospective study was approved with a waiver for the requirement of patients' informed consent by Clinical Research Ethics Committee of Shandong Provincial Hospital (SWYX2024-194). No one received any compensation or incentive for the participation in the present study.

**MDCTA image acquisition and processing**

MDCTA (Definition Flash; Siemens Healthcare, Forchheim, Germany) was performed for all potentially eligible patients for a meticulous diagnosis of CoA. The scans were performed in cranio-caudal direction, extending from the thoracic inlet to the diaphragm, with images acquired at 40% R-R interval and a slice thickness of 1.0mm. The following morphological characteristics were recorded: (1) maximum diameters of the posterior transverse arch (D1), isthmus (D2), and distal coarcted descending aorta (D3) (Figure 1); (2) distribution of collateral branches; and (3) presence of other intracardiac malformations.

**Doppler echocardiography**

Pre- and post-operative Doppler echocardiography (Philips iE 33 imaging system or Philips Epiq 7c Ultrasound System, Philips Healthcare, Andover, Massachusetts, USA) was utilized to acquire the following patient-specific data at the end of systole: forward flow velocity of the aortic valve ($V_{Ao}$, m/s), descending aortic coarctation velocity, and left ventricular ejection fraction (LVEF, %), and diameters, forward flow velocities, and peak systolic pressure difference (PSPD, mmHg) at the ostia of the brachiocephalic trunk, the left common carotid, and the left subclavian arteries. Abdominal and femoral artery flows were also assessed.

**Cardiac catheterization**

Under general anesthesia, via femoral artery, the coarctation was crossed with a coronary guidewire, and invasive gradients were measured. And then a cheatham-platinum (CP) stent was positioned after pre-dilatation with angioplasty balloon, and gently dilated within the coarctation. The size of the CP stent or angioplasty balloon

was chosen according to the measurements. The perfect positioning of the stent and correction of the coarctation was confirmed by a control aortography.

**Construction of the aorta and mesh generation**

Geometrically representative patient-specific 3D computer models, with ascending aorta, aortic arch and branches, descending aorta and abdominal aorta retained, were semi-automatically segmented and reconstructed from MDCTA raw data using Mimics 21.0 software (Materialise NV, Leuven, Belgium) and optimized using 3-matic 11.0 and Magics 22.0 (Materialise NV, Leuven, Belgium). A schematic workflow of the MDCTA-based CFD method was demonstrated in Figure 2. The mesh generation was based on the 3D geometric models using an automatic mesh generation software (Ansys ICEM 14.5, ANSYS, Inc., Canonsburg, Pennsylvania, USA).

**Mesh independence study**

Patient-specific computational meshes were generated for all models. Mesh quality was rigorously assessed, ensuring that over 85% of elements achieved a quality index (QI) greater than 0.85, with QI exceeding 0.9 in hemodynamically critical regions such as the coarctation site.

A grid independence study was performed on a representative case (Patient #5). Three meshes of increasing density (coarse, medium, fine) were generated. The medium mesh satisfied convergence criteria for the PG, with a grid convergence index (GCI) of 2.8% and a relative difference of <5% compared to the fine mesh. The medium mesh density was therefore adopted for all simulations to balance accuracy and computational efficiency. Detailed mesh parameters for all patients are summarized in Table 2.

**Computational fluid dynamics simulations**

Steady-state (peak-systole) simulation was performed by using Ansys FLUENT 19.0 (Fluent Inc., Lebanon, New Hampshire, USA). Blood was assumed to be an incompressible, laminar, Newtonian fluid with a density (ρ) of 1050 kg/m$^3$ and dynamic viscosity ($\mu$) of $3.5\times10^{-3}$Pa·s [16, 23-25]. The aortic wall was considered as rigid with no-slip conditions. The governing Navier-Stokes equations were solved using the SIMPLEC algorithm:

$$\rho\,(\mathrm{u}\cdot\nabla\mathbf{u}) = -\nabla p + \mu\,\nabla^2\mathbf{u}, \quad \nabla\cdot\mathbf{u} = 0$$

where $\mathbf{u}$ is velocity and $p$ is pressure. Peak-systolic wall shear stress (WSS) was computed as:

$$\tau_w = \mu\left(\frac{\partial u}{\partial n}\right)_{wall}$$

**Boundary conditions**

Inlet (AAO): A steady velocity condition ($U_{in}$) was applied, derived from Doppler-measured peak aortic valve velocity ($V_{Ao}$) using a scaling factor: $U_{in} = \alpha * V_{Ao}$. A value of $\alpha = 0.7$ was selected as a physiologically plausible estimate for large-artery systolic flow and conducted a sensitivity analysis over the range $\alpha = 0.6$-$0.8$ (see supplementary materials for details).

Outlets: Patient-specific steady pressure targets were prescribed. For each outlet $i$, the target pressure $P_{out,\,i}$ was calculated as: $P_{out,\,i} = \text{Cuff\_SBP}_{limb,i} + \text{PSPD}_i$, where $\text{Cuff\_SBP}_{limb,i}$ is the systolic cuff pressure from the corresponding extremity, and PSPD is the peak systolic pressure difference at the vessel ostium estimated from Doppler velocities using the simplified Bernoulli equation ($PSPD = 4 * V^2$). This approach, under the peak-systolic steady-state assumption, is conceptually equivalent to defining an effective resistance at each outlet, derived from a lumped parameter model (LPM) where capacitive effects are negligible (Figure 3, Table 5).

The primary simulation output, the trans-coarctation PG (ΔP), was extracted and validated against invasive catheterization measurements.



**Statistical analysis**

For statistical analysis, quantitative data were reported as mean ± SD and compared with Paired Student's t-test or Wilcoxon signed-rank test, as appropriate after testing normality. Qualitative data were expressed as percentages. Intra-class correlation coefficients (ICCs) with 95% confidence intervals were calculated to determine inter-and intra-observer variability for aortic arch dimension measurements, with ICCs greater than 0.8 as an indicator of excellent reproducibility between two experienced readers. The agreement between the values was investigated using Bland-Altman plots. The Pearson's $r$ coefficient was performed to compute the linear relation between the values. Data were analyzed using SPSS 20.0 software (SPSS, Chicago, IL, USA) and MedCalc 15.8 (MedCalc Software bvba, Ostend, Belgium). $p<0.05$ were considered to be statistically significant.

**Results**

**Patient characteristics and arch dimensions**

18 patients with CoA, including 11 males and 7 females, at mean age 20.70 ± 11.10 years (mean ± SD), were included in this study. All 18 patients underwent pre- and post-intervention Doppler echocardiography with interval time of 2.7 ± 1.2 days (mean ± SD) and intervention. 11 patients received pre- and post-intervention MDCTA with interval time of 4.3 ± 1.0 days (mean ± SD), and post-

intervention MDCTA data of the rest 7 patients were not available due to loss of follow-up. A total of thirty-one patient-specific 3D models were generated for the eighteen patients. Patient characteristics and pre-interventional morphologic parameters of the aortic arch from MDCTA were listed in Table 1. ICCs were calculated to test inter-and intra-observer agreement for the morphological values. And ICC values for measurements between observers were greater than 0.831, indicating excellent reliability (Table 3).

The measured systolic BPs in the upper arm were 162.6 ± 17.8 mmHg (left), and 165.8±22.8mmHg (right), and in the lower limb were 107.5±17.3 mmHg (left), and 114.7±15.3 mmHg (right), with a mean arm-ankle blood pressure difference (AABPD) of 55.1±15.3 (left) or 51.1±21.5mmHg (right). After intervention, BPs in the upper left and right limb significantly decreased to 126.2±13.1 and 127.1±12.2mmHg respectively ($p$<0.01), and the decrease in BPs in the lower limb was not remarkable ($p$>0.05). The measured AABPD significantly declined to 12.0±9.68 (left) or 12.0±11.1 mmHg (right) ($p$<0.01). Post-operative inter-arm systolic blood pressure difference (IASBPD) (mmHg) was not significantly reduced as compared to pre-operative data (0.88±4.98 vs. 3.2±10.8, $p$>0.05) (Supplementary Figure S2). Intervention did not significantly alter the average LVEF (%) (60.9±1.4 vs.62.1±1.6, $p$>0.05), but it did reduce the levels of serum creatinine (56.9±15.6 vs. 60.7±14.5, $p$<0.01), with increased eGFR (133.2±26.5 vs. 123.7±25.1, $p$<0.05), as compared to pre-intervention data (Supplementary Figure S3). Table 4 showed measured patients' characteristics included four-limb blood pressure, LVEF, the biochemical and physiological indexes before and after intervention.

**Validation**

The non-invasively computed trans-coarctation PGs were calculated from the proposed algorithm, and compared with the clinical gold-standard cardiac catheter pressure measurements in patients investigated in this study. Doppler echocardiography-derived gradients were also compared with the catheter measurements. Pre-treatment results showed that the PG measured by Doppler or the catheter was 57.78±18.02mmHg or 55.72±19.71 mmHg, respectively, and computed PG based on the LPM CFD was 58.44±17.77 mmHg. The post-intervention data indicated that PGs measured by Doppler, the catheter or from our CFD model was 20.61±7.43, 15.65±5.15, or 17.94±10.54mmHg accordingly.

Bland-Altman test demonstrated good qualitive agreement between PG (including pre- and post-intervention data) measured by CFD and catheter. The bias was 2.5±4.94 mmHg with a 95% confidence interval (CI) of -0.47 to 5.45 mmHg. The lower and upper

limits of agreement are -12.75 (95% CI: -17.88– -7.64) and 17.74 (95% CI: 12.63–22.86) mmHg, respectively (Figure 4a). There was also good qualitive agreement between pre-treatment PG measured by CFD and catheter using the Bland-Altman plot. The bias was -2.72±5.24 mmHg with a 95% confidence interval (CI) of -7.14 to 17.0 mmHg. The lower and upper limits of agreement are -20.14 (95% CI: -27.85– -12.45) and 14.70 (95% CI: 7.00–22.40) mmHg correspondingly (Figure 4b). Pearson's *r* correlation analysis implicated a significant relationship between the pretreatment catheter-measured pressure drops and those computed based on our CFD simulation (r=0.89, and $p< 0.05$). And there was also a strong linear correlation between the post-treatment catheter pressure drops and those computed based on the CFD simulation (r=0.90, and $p<0.05$).

The Bland-Altman agreement test also showed agreement between PGs measured by Doppler and the catheter (Figure 4c). The bias was 3.46±7.69 mmHg with a 95% confidence interval (CI) of -0.72 to 7.65 mmHg. The lower and upper limits of agreement are -20.41 (95% CI: -27.63– -13.19) and 27.34 (95% CI: 20.12–34.57) mmHg correspondingly. While, the Pearson's *r* correlation analysis indicated a relatively weak relationship between pressure drops measured by Doppler and the catheter, either before (r=0.71, and $p>0.05$) or after the intervention (r=0.30, and $p >0.05$). Figure 5 and Figure 6 showed examples of the cases (patient #1 and #2), where the simulated PGs of the CoA correlated well with catheter measurements with a maximum mean relative error (MRE) of 13.6%, whereas a maximum MRE of 60% was reported for PG from Doppler estimates against catheter measurements.

**Hemodynamics**

Hemodynamic distributions derived from different boundary conditions were generated. Flow visualization showed that at the peak-systolic instant, the streamline distributed similar to laminar flow in ascending and transverse arch in all most all cases, except for patient #3 of hypoplastic aortic arch, where the maximum flow velocity was localized at inner wall of aortic arch/lesser aortic arch curvature and the coarctation. CoA presence altered substantially the flow dynamics and caused vortical structure in the aorta. Peak/highest flow velocity of the disturbed flow was observed at the CoA, and the helical streamline pattern was observed at peak systole at the distal wall of descending aorta (Supplementary Figure S4), except for patient #2 of diffuse narrowing of the descending aorta. After the correction of the CoA, the flow pattern became smooth and more attached to the wall with maximum flow velocities

moved to the proximal aorta and inner wall of aortic arch/lesser aortic arch curvature. (Figure 5)

Pressure distribution was another major hemodynamic force. With a unified color scale, the wall-pressure maps suggest a reduction in the high-pressure region proximal to the coarctation after intervention (Figure 5,6,7). At peak systole, the surface area-weighted mean wall static (gauge) pressure over the reconstructed aortic model decreased from 164.67±76.79 mmHg (pre-intervention) to 116.55 ± 44.43mmHg (post-intervention). The pressures were introduced in the lateral walls of ascending aorta root, supra aortic branches and upstream of the coarctation. And negative intravascular pressures were indicated at the CoA. Such uneven pressures were altered by the intervention, as documented by the simulations, where peak systolic pressure was noted at the lateral wall of the ostia of supra aortic branches, with the range also narrowed down and negative intravascular pressures at the CoA turned positive.

Peak systolic wall shear stress (PSWSS) was also evaluated (123.13±96.60 vs. post-intervention 64.91±37.25 Pa). Before the intervention, the highest PSWSS was localized at the CoA, with a distribution similar to the flow velocity, followed by transverse arch and the ostia of supra aortic branches. Reduced PSWSS were observed after the intervention, with a maximum reduction of 44% in patient #5 (Figure 7), except for patient #2, where a stent was deployed, and the highest PSWSS was localized at left wall of the stent and outer wall of ostium of left subclavian artery (Figure 6). PSWSS distribution was similar to the maximum flow velocity.



**Discussion**

Accurate non-invasive quantification of trans-coarctation pressure gradients remains a clinical challenge, largely due to the difficulty of defining physiologically consistent boundary conditions in CFD simulations. Alterations of hemodynamics in the aorta are closely associated with aortic pathologies such as aneurysms and stenosis, which adversely affect the long-term outcomes of these patients of CoA, primarily through abnormal pressure gradients and flow disturbances [26-28]. Early diagnosis and intervention are of critical significance for managing the disease and associated complications. In recent years, a number of CFD models have been investigated to analyze the hemodynamics in CoA patients [20]. The accurate assessment of the CoA was dependent on appropriate choice of CFD models and defining appropriate boundary conditions [20, 29-33], where parameter inputs at the inlet(s) and outlet(s) are crucial to ensure accuracy and validity of numerical solutions in CFD simulations [23, 32, 34-36].

In previous studies, several CFD models were based on model parameters and/or boundary conditions relied on invasively acquired pressures or flows, which limits clinical scalability and constrains truly non-invasive application. [23]. Rafieianzab et al [37] developed a non-invasive fluid-solid interaction (FSI) model to quantify both global and local hemodynamical variables across CoA with varying severities, implicating the inclusion of the vessel wall may have great impacts on the blood flow parameters and wall shear stress indices, but their broader clinical adoption remains limited by computational cost and the need for further large-scale validation. Four-dimensional (4D) flow MRI studies have been proposed to provide valuable parameters during CFD simulation, such as deranged helix or vortex flow and elevated peak velocities, which are assumed to correlate with the development of aortic dilation and aneurysms [38]. However, challenges such as low spatiotemporal resolution and phase-offset artifacts have hindered its clinical application of 4D flow MRI [39], and these required data from 4D MRI are often not routinely collected in the clinical setting [40], potentially incurring additional costs.

Doppler echocardiography data have been integrated into the inlets and outlets of CFD models in recent years [4, 41]. Importantly, we established a patient-specific, non-invasive CFD framework. Rather than employing a complex, time-resolved (pulsatile) cardiovascular model, our approach utilizes a simplified electrical circuit analogy to define boundary conditions at the peak-systolic instant. Under the quasi-steady operating point ($dP/dt \approx 0$), each three-element Windkessel outlet reduces to an effective resistive load, which is consistent with the prescribed pressure-outlet formulation. Specifically, the inlet boundary condition was defined using peak systolic aortic velocity measured by Doppler echocardiography. Outlet pressures were prescribed using limb cuff blood pressures, further adjusted by Doppler-derived peak systolic pressure differences (PSPDs) measured at the corresponding arterial ostia. The above-mentioned parameters are not limited by the poor acoustic windows, resulting in very little error and being easy to obtain. Different from previous studies [7], where the data collection was not simultaneously and mean arterial pressure was relied on, our data were collected within a one-week timeframe, and PSPD at the end of systole were used to obtain the boundary conditions at the outlets of left common carotid artery, brachiocephalic or left subclavian artery. The collection of the inlet and outlet data was feasible, convenient and non-invasive. At the peak-systolic operating point, the capacitive branch of the three-element Windkessel model becomes inactive, such that each outlet reduces to an effective

resistive load consistent with the imposed pressure-outlet boundary condition. Our CFD model indicated pre- and post-intervention peak pressure drop differs of 2.7 and 2.1 mmHg. The higher pressure difference in the CFD simulations might be attributed to : (1) the inlet being determined by the forward flow velocity of the aortic valve, when segmentation was initiated distant from the sinotubular junction during modeling, leading to potential overestimation of the inflow velocity; (2) cuff BP measurements taken without sedation, while intra-operational radial and femoral artery pressure were obtained under anesthesia, which might yield lower readings, although patients with lower extremity arterial thrombosis were excluded; (3) small collateral arteries were excluded from manual segmentation, despite the exclusion of CoA patients with presence of PDA and extensive collateral circulation, which might lead to overestimations; (4) Furthermore, the assumption of Newtonian blood behavior, while common in large-artery hemodynamics, may overestimate viscous forces in the stenotic region where shear rates are highest, potentially contributing to a slight overestimation of the computed pressure gradient. Prior literature indicated a variation of 5-10mmHg during cardiac catheterization measurements due to impacts of inspiration and expiration [7], suggesting that our results reflected an acceptable degree of variability in the clinical setting. From this standpoint, the CFD results from our algorism showed good agreements with the cardiac catheterization measurements. Next, we compared Doppler estimated pressure difference against those from catheter measurements. In accordance with previous studies [42], our findings indicated greater discrepancies between Doppler estimates and catheter measurements, consistent with prior studies, Doppler-derived pressure gradients exhibited a tendency toward overestimation relative to catheter measurements. This discrepancy, on one hand, might be correlated with patient-specific conditions and techniques employed by sonographers during Doppler examination, and on the other hand, the Bernoulli equation neglected the velocity distribution across the coarctation plane, leading to a consistent overestimation of pressure drops due to reliance on a single peak velocity from non-uniform velocity profiles across the coarctation site [43].

The presence of CoA exerted a great influence on hemodynamic patterns. In the present study, we included patients with severe CoA, and our CFD simulations demonstrated disturbed streamline distribution with peak flow velocities at the inner wall of the coarctation and helical flows at the distal wall of descending aorta. This high speeding blood flow substantially impacted the arterial wall, which might introduce increased aortic pulse wave velocity,

intima-media thickness and circumferential wall stress, associated with enhanced aortic stiffness and wall thickness, thereby leading to high risk for early atherosclerosis, dilation of the aorta and formation of aneurysm. [44-46] Following the repair of the CoA, CFD simulations revealed a return to a smoother flow pattern, which was more attached to the wall, with maximum flow velocities shifting to the proximal aorta and the inner wall of the aortic arch/lesser aortic arch curvature, while the helical flow reduced or disappeared. Preoperative simulations illustrated that the presence of CoA led to elevated peak systolic pressures upstream of the coarctation, increased cardiac preload, and negative intravascular pressure at the CoA, which might be attributed to high velocities of the blood, and might lead to further collapse of the arterial wall at the coarctation and the development of heart failure. [46, 47] After the intervention, negative intravascular pressure at the CoA area was resolved, and peak systolic pressures were reduced. Notably, at the ostia of the aortic branches, we observed higher PSWSS in areas against the flow direction, which might account for the susceptibility of cervical artery to atherosclerosis [48, 49].

Furthermore, our results indicated that intervention of CoA caused decrease in serum creatinine levels and elevation of eGFR levels, although no significant alterations of LV function were noted, implicating that improved aortic hemodynamics also positively influenced local perfusion of the kidneys.

**Study Limitations**

First, the CFD analysis was performed under an instantaneous steady-state (peak-systolic) assumption to estimate PG of CoA, which cannot simulate the pulsatile variations in downstream pressure throughout the cardiac cycle. Accordingly, the 3-element Windkessel model effectively reduces to a resistive load at the operating point (□□/□□≈0), and outlet compliance cannot be independently identified. Second, peak-systolic outlet pressure targets were constructed from cuff pressures and Doppler-derived; because these measurements may not be perfectly simultaneous, physiologic variability (e.g., heart rate, autonomic tone, loading conditions) can introduce boundary-condition uncertainty. Third, Newtonian blood rheology and rigid walls were assumed, which may affect viscous losses and shear metrics. Fourth, age-related differences in vascular stiffness are not explicitly modeled beyond patient-specific geometry and measurement-driven pressures, so inferred outlet loads should be interpreted as effective peak-systolic resistances. Finally, segmentation, mesh resolution in stenotic regions, and velocity-to-mean conversion assumptions may contribute to residual discrepancies versus catheterization. The current workflow requires

approximately 3-4 hours of processing time per case, which positioned as a tool for delayed decision support precludes rather than for immediate diagnostic assessment.

## Conclusion

We developed a multimodal, patient-specific framework that couples computational fluid dynamics (CFD) informed by a lumped-parameter circuit framework. Using CTA-derived anatomy together with Doppler ultrasound and limb cuff pressures, peak-systolic simulations estimated trans-coarctation pressure gradients and provided full-field pressure, velocity, and wall shear stress metrics. In 18 patients studied pre- and post-intervention, the CFD–LPM approach showed strong agreement with catheterization and improved robustness compared with Doppler-only gradients, supporting its use as a practical adjunct for individualized assessment and planning.

## Acknowledgments

H.W. and Y.Z. conceptualized the manuscript. M.H., X.L. and H.W. participated in data collection. M.H., X.L., H.W. and Y.Z. conducted the data analysis and wrote the manuscript. X.W., J.L., Z.M., P.G. and X.S. contributed to revision of the manuscript. All authors reviewed the manuscript.

## Sources of Funding

This work was supported by Natural Science Foundation of Shandong Province (Grant No. ZR2022MH227) and Key R&D Program (Soft Science Project) of Shandong Province, China (Grant No. 2022CXGC010504).

## Data availability statement

Data available within the article or its supplementary materials.

## Disclosures

The authors declare no competing interest.

## REFERENCES

1. Shih, M.C., et al., Surgical and endovascular repair of aortic coarctation: normal findings and appearance of complications on CT angiography and MR angiography. AJR Am J Roentgenol, 2006. **187**(3): p. W302-12.
2. Salciccioli, K.B. and J.P. Zachariah, Coarctation of the Aorta: Modern Paradigms Across the Lifespan. Hypertension, 2023. **80**(10): p. 1970-1979.

3. Chetan, D. and L.L. Mertens, Challenges in diagnosis and management of coarctation of the aorta. Curr Opin Cardiol, 2022. **37**(1): p. 115-122.
4. Keshavarz-Motamed, Z., et al., Elimination of Transcoarctation Pressure Gradients Has No Impact on Left Ventricular Function or Aortic Shear Stress After Intervention in Patients With Mild Coarctation. JACC Cardiovasc Interv, 2016. **9**(18): p. 1953-65.
5. Nguyen, L. and S.C. Cook, Coarctation of the Aorta: Strategies for Improving Outcomes. Cardiol Clin, 2015. **33**(4): p. 521-30, vii.
6. Bhatt, A.B. and D. Defaria Yeh, Long-term outcomes in coarctation of the aorta: an evolving story of success and new challenges. Heart, 2015. **101**(15): p. 1173-5.
7. Aslan, S., et al., Non-invasive Prediction of Peak Systolic Pressure Drop across Coarctation of Aorta using Computational Fluid Dynamics. Annu Int Conf IEEE Eng Med Biol Soc, 2020. **2020**: p. 2295-2298.
8. Dijkema, E.J., T. Leiner, and H.B. Grotenhuis, Diagnosis, imaging and clinical management of aortic coarctation. Heart, 2017. **103**(15): p. 1148-1155.
9. Jenkins, N.P. and C. Ward, Coarctation of the aorta: natural history and outcome after surgical treatment. Qjm, 1999. **92**(7): p. 365-71.
10. Brickner, M.E., L.D. Hillis, and R.A. Lange, Congenital heart disease in adults. First of two parts. N Engl J Med, 2000. **342**(4): p. 256-63.
11. Uematsu, Manabu et al. “Direct Angioscopic and Serial Computed Tomographic Observations of the Progression of Atypical Aortic Coarctation Leading to Heart Failure.” The Canadian journal of cardiology,S0828-282X(25)00370-8.20 May.2025.
12. Shi, Y., et al., Patient-specific non-invasive estimation of pressure gradient across aortic coarctation using magnetic resonance imaging. J Cardiol, 2019. **73**(6): p. 544-552.
13. Karaosmanoglu, A.D., et al., CT and MRI of aortic coarctation: pre- and postsurgical findings. AJR Am J Roentgenol, 2015. **204**(3): p. W224-33.
14. Leo, I., et al., Non-Invasive Imaging Assessment in Patients with Aortic Coarctation: A Contemporary Review. J Clin Med, 2023. **13**(1).
15. Nair, Priya J et al. “Non-invasive estimation of pressure drop across aortic coarctations: validation of 0D and 3D computational models with in vivo measurements.” medRxiv :

the preprint server for health sciences 2023.09.05.23295066. 6 Sep. 2023, doi:10.1101/2023.09.05.23295066. Preprint.
16. Brüning, J., et al., Uncertainty Quantification for Non-invasive Assessment of Pressure Drop Across a Coarctation of the Aorta Using CFD. Cardiovasc Eng Technol, 2018. **9**(4): p. 582-596.
17. Seifert, B.L., et al., Accuracy of Doppler methods for estimating peak-to-peak and peak instantaneous gradients across coarctation of the aorta: An In vitro study. J Am Soc Echocardiogr, 1999. **12**(9): p. 744-53.
18. Nair PJ, Pfaller MR,et al. Non-invasive Estimation of Pressure Drop Across Aortic Coarctations: Validation of 0D and 3D Computational Models with In Vivo Measurements. Ann Biomed Eng. 2024;52(5):1335-1346.
19. LaDisa, J.F., Jr., et al., Computational simulations for aortic coarctation: representative results from a sampling of patients. J Biomech Eng, 2011. **133**(9): p. 091008.
20. Arzani, A., et al., In vivo validation of numerical prediction for turbulence intensity in an aortic coarctation. Ann Biomed Eng, 2012. **40**(4): p. 860-70.
21. Bonfanti, M., et al., Patient-specific haemodynamic simulations of complex aortic dissections informed by commonly available clinical datasets. Med Eng Phys, 2019. **71**: p. 45-55.
22. Stout, K.K., et al., 2018 AHA/ACC Guideline for the Management of Adults With Congenital Heart Disease: A Report of the American College of Cardiology/American Heart Association Task Force on Clinical Practice Guidelines. Circulation, 2019. **139**(14): p. e698-e800.
23. Goubergrits, L., et al., MRI-based computational fluid dynamics for diagnosis and treatment prediction: clinical validation study in patients with coarctation of aorta. J Magn Reson Imaging, 2015. **41**(4): p. 909-16.
24. Mirzaee, H., et al., MRI-based computational hemodynamics in patients with aortic coarctation using the lattice Boltzmann methods: Clinical validation study. J Magn Reson Imaging, 2017. **45**(1): p. 139-146.
25. Goubergrits, L., et al., Patient-specific requirements and clinical validation of MRI-based pressure mapping: A two-center study in patients with aortic coarctation. J Magn Reson Imaging, 2019. **49**(1): p. 81-89.
26. Ladisa, J.F., Jr., C.A. Taylor, and J.A. Feinstein, AORTIC COARCTATION: RECENT DEVELOPMENTS IN EXPERIMENTAL AND COMPUTATIONAL METHODS TO ASSESS TREATMENTS FOR THIS SIMPLE CONDITION. Prog Pediatr Cardiol, 2010. **30**(1): p. 45-49.

27. Midulla, M., et al., Haemodynamic imaging of thoracic stent-grafts by computational fluid dynamics (CFD): presentation of a patient-specific method combining magnetic resonance imaging and numerical simulations. Eur Radiol, 2012. **22**(10): p. 2094-102.
28. Vergara, C., et al., Influence of bicuspid valve geometry on ascending aortic fluid dynamics: a parametric study. Artif Organs, 2012. **36**(4): p. 368-78.
29. Gallo, D., et al., On the use of in vivo measured flow rates as boundary conditions for image-based hemodynamic models of the human aorta: implications for indicators of abnormal flow. Ann Biomed Eng, 2012. **40**(3): p. 729-41.
30. Jin, S., J. Oshinski, and D.P. Giddens, Effects of wall motion and compliance on flow patterns in the ascending aorta. J Biomech Eng, 2003. **125**(3): p. 347-54.
31. Kousera, C.A., et al., A numerical study of aortic flow stability and comparison with in vivo flow measurements. J Biomech Eng, 2013. **135**(1): p. 011003.
32. Morbiducci, U., et al., Inflow boundary conditions for image-based computational hemodynamics: impact of idealized versus measured velocity profiles in the human aorta. J Biomech, 2013. **46**(1): p. 102-9.
33. Armour, C.H., et al., The influence of inlet velocity profile on predicted flow in type B aortic dissection. Biomech Model Mechanobiol, 2021. **20**(2): p. 481-490.
34. Lin, S., et al., Fluid-Structure Interaction in Abdominal Aortic Aneurysm: Effect of Modeling Techniques. Biomed Res Int, 2017. **2017**: p. 7023078.
35. Pirola, S., et al., Computational study of aortic hemodynamics for patients with an abnormal aortic valve: The importance of secondary flow at the ascending aorta inlet. APL Bioeng, 2018. **2**(2): p. 026101.
36. Youssefi, P., et al., Impact of Patient-Specific Inflow Velocity Profile on Hemodynamics of the Thoracic Aorta. J Biomech Eng, 2018. **140**(1).
37. Rafiei, D., et al., The effect of coarctation degrees on wall shear stress indices. Sci Rep, 2021. **11**(1): p. 12757.
38. Desai, L., et al., Four-Dimensional flow Magnetic Resonance Imaging for Assessment of Pediatric Coarctation of the Aorta. J Magn Reson Imaging, 2022. **55**(1): p. 200-208.
39. Fathi, M.F., et al., Super-resolution and denoising of 4D-Flow MRI using physics-Informed deep neural nets. Comput Methods Programs Biomed, 2020. **197**: p. 105729.

40. Mercuri, M., et al., Subject-specific simulation for non-invasive assessment of aortic coarctation: Towards a translational approach. Med Eng Phys, 2020. **77**: p. 69-79.
41. Swanson, L., et al., A Patient-Specific CFD Pipeline Using Doppler Echocardiography for Application in Coarctation of the Aorta in a Limited Resource Clinical Context. Front Bioeng Biotechnol, 2020. **8**: p. 409.
42. Zhang, M., et al., CTA-Based Non-invasive Estimation of Pressure Gradients Across a CoA: a Validation Against Cardiac Catheterisation. J Cardiovasc Transl Res, 2021. **14**(5): p. 873-882.
43. Donati, F., et al., Beyond Bernoulli: Improving the Accuracy and Precision of Noninvasive Estimation of Peak Pressure Drops. Circ Cardiovasc Imaging, 2017. **10**(1): p. e005207.
44. Ververs, F.A., et al., Preclinical Aortic Atherosclerosis in Adolescents With Chronic Disease. J Am Heart Assoc, 2022. **11**(14): p. e024675.
45. Krishnamurthy, Y., et al., Subclinical Burden of Coronary Artery Calcium in Patients With Coarctation of the Aorta. Am J Cardiol, 2019. **123**(2): p. 323-328.
46. Kartal Öztürk, G., et al., Evaluation of increased arterial stiffness in pediatric patients with cystic fibrosis by augmentation index and pulse wave velocity analysis. Pediatr Pulmonol, 2020. **55**(5): p. 1147-1153.
47. Coogan, J.S., et al., Computational fluid dynamic simulations for determination of ventricular workload in aortic arch obstructions. J Thorac Cardiovasc Surg, 2013. **145**(2): p. 489-495.e1.
48. Timmins, L.H., et al., Focal association between wall shear stress and clinical coronary artery disease progression. Ann Biomed Eng, 2015. **43**(1): p. 94-106.
49. Andersson, M., T. Ebbers, and M. Karlsson, Characterization and estimation of turbulence-related wall shear stress in patient-specific pulsatile blood flow. J Biomech, 2019. **85**: p. 108-117.

**Table 1**
**Patient characteristics and pre-interventional morphologic parameters of the aortic arch from MDCTA.**

| Cases | Sex | Age (years) | D1 (cm) | D2 (cm) | D3 (cm) | CoA length (cm) | Interventional treatments |
|---|---|---|---|---|---|---|---|
| No.1 | Female | 14 | 3.5×3.2 | 1.3×1.2 | 3.0×2.6 | 0.6 | BIB catheter dilation+ stent |
| No.2 | Male | 16 | 3.7 | 0.9 | 1.0 | 3.6 | Balloon dilation |
| No.3 | Male | 6 | 1.21 | 1.0×0.8 | 2.1×1.9 | 2.25 | Balloon dilation |
| No.4 | Female | 22 | 1.5 | 0.6×0.5 | 3.0 | 4 | BIB catheter dilation+ CP stent |
| No.5 | Male | 16 | 1.3 | 0.19 | 1.4 | 3.5 | BIB balloon dilation+ CP stent |

| | | | | | | | |
|---|---|---|---|---|---|---|---|
| No.6 | Female | 29 | 3.2×3.2 | 0.61 | 0.95×0.95 | 3.77 | CP stent |
| No.7 | Male | 32 | 1.7 | 0.7 | 4.2 | 2.1 | BIB catheter dilation+ stent |
| No.8 | Female | 20 | 1.6 | 0.6 | 3.3 | 4.0 | BIB catheter dilation+ stent |
| No.9 | Male | 40 | 3.1×3.0 | 0.8×0.6 | 1.6×1.7 | 3.0 | CP stent |
| No.10 | Female | 13 | 2.0 | 0.56 | 2.9 | 2.3 | Balloon dilation |
| No.11 | Male | 16 | 3.2 | 0.43 | 3.37 | 1.90 | BIB catheter dilation+ stent |
| No.12 | Male | 7 | 1.34 | 0.65 | 2.1 | 1.89 | Balloon dilation |
| No.13 | Male | 49 | 4.1 | 1.23 | 4.32 | 2.31 | BIB catheter dilation+ stent |
| No.14 | Male | 23 | 2.90 | 1.23 | 3.23 | 1.67 | CP stent |
| No.15 | Male | 9 | 2.45 | 0.99 | 2.95×3.0 | 2.1 | Balloon dilation |
| No.16 | Female | 19 | 3.11 | 1.45 | 3.12 | 1.33 | CP stent |
| No.17 | Male | 23 | 2.98 | 1.09 | 3.78 | 2.11 | CP stent |
| No.18 | Female | 19 | 3.12 | 1.33 | 2.76 | 1.67 | BIB catheter dilation+ stent |

D1: maximum diameters of the posterior transverse arch; D2 maximum diameters of isthmus; D3: distal coarcted descending aorta; BIB: balloon in balloon; CP: cheatham-platinum



**Table 2**

**Mesh details of all Patient.**

| Cases | | Number of Elements | |
|---|---|---|---|
| | | Pre-intervention | Post-intervention |
| **No.1** | | 2720270 | 3450987 |
| **No.2** | | 1715637 | 2219870 |
| **No.3** | | 2761918 | 3005065 |
| **No.4** | | 5271231 | - |
| **No. 5** | Coarse | 1819196 | 5992477 |
| | Fine | 5302881 | |

| | | |
|---|---|---|
| Refined | 7999464 | |
| **No.6** | 3378190 | 4267781 |
| **No.7** | 2097610 | - |
| **No.8** | 3901456 | 4002398 |
| **No.9** | 4923709 | - |
| **No.10** | 2793026 | 3317011 |
| **No.11** | 6510455 | 6901986 |
| **No.12** | 5017621 | - |
| **No.13** | 4903657 | - |
| **No.14** | 3996708 | 4602361 |
| **No.15** | 2904489 | - |
| **No.16** | 2290643 | 3872460 |
| **No.17** | 3804383 | - |
| **No.18** | 5610934 | 6346898 |

-: Patient lost to follow-up.

**Table 3**

**Inter-and intra-observer agreement for the morphological values.**

| Parameters | Inter-observer | | Intra-observer | |
|---|---|---|---|---|
| | ICC | 95%CI | ICC | 95%CI |
| D1 | 0.969 | (0.871-0.993) | 0.975 | (0.967-0.986) |
| D2 | 0.831 | (0.419-0.959) | 0.965 | (0.917-0.980) |
| D3 | 0.982 | (0.923-0.996) | 0.975 | (0.977-0.992) |
| CoA length | 0.991 | (0.959-0.998) | 0.971 | (0.958-0.989) |

D1: maximum diameters of the posterior transverse arch; D2 maximum diameters of isthmus; D3: distal coarcted descending aorta; CI: confidence interval.

**Table 4**

**Pre- and post-interventional biochemical and physiological indexes.**

| | Pre-intervention | Post-intervention | P value |
|---|---|---|---|

| | | | | |
|---|---|---|---|---|
| BP (mmHg) | Left upper arm | 162.6±17.9 | 126.2±13.1 | <0.001 |
| | Right upper arm | 165.8±22.8 | 127.1±12.2 | <0.001 |
| | Left lower limb | 107.5±17.3 | 114.2±15.3 | 0.109 |
| | Right lower limb | 114.7±15.3 | 115.1±15.1 | 0.945 |
| BPD (mmHg) | Left AABPD | 55.1±15.3 | 12.0±9.68 | <0.001 |
| | Right AABPD | 51.1±21.5 | 12.0±11.1 | <0.001 |
| | IASBPD | 3.2±10.8 | 0.88±4.98 | 0.486 |
| LVEF (%) | | 62.1±1.6 | 60.9±1.4 | 0.179 |
| Serum creatinine (μmol/L) | | 60.7±14.5 | 56.9±15.6 | 0.007 |
| eGFR (mL/(min·1.73m$^2$)) | | 123.7±25.1 | 133.2±26.5 | 0.041 |
| Blood urea nitrogen (mmol/L) | | 5.11±0.77 | 4.58±1.15 | 0.060 |

AABPD: arm-ankle blood pressure difference; IASBPD: inter-arm blood pressure difference



**Table 5. Summarized cardiovascular parameters used in the LPM coupled with CFD**

| Category | Symbol | Definition / Formula | Physiological meaning | Role in this study |
|---|---|---|---|---|
| **Inlet flow** | $Q_{in}$ | $Q_{in} = U_{in} A_{in}$ | Ascending aortic volumetric inflow at peak systole | CFD inlet flow boundary |
| | $U_{in}$ | Area-averaged inlet velocity | Mean systolic inflow velocity | Derived from Doppler with correction |
| | $A_{in}$ | CTA-derived inlet area | Cross-sectional area of ascending aorta | Geometry-based |
| **Pressures** | $P_{in}$ | | Peak systolic ascending aortic pressure | Constructed from cuff BP + PSPD |
| | $P_{out,\ i}$ | Prescribed | Outlet peak systolic pressure | Pressure-outlet BC |
| | $P_v$ | Reference pressure | Venous reference pressure | Common downstream reference |

| | | | | |
|---|---|---|---|---|
| **Flow conservation** | $Qi$ | $\int_{Ai} u \cdot n \cdot \partial A$ | Branch flow rate | CFD-computed |
| | — | Qin=Q1+Q2+Q3+Q4 | Mass conservation | Closed-loop consistency |
| **Outlet load (3WK)** | $R$ t, i | (ΔP i=Rt,iQ_i) | Effective outlet resistance | Active load at peak systole |
| | $R$ p, i | Proximal resistance | Characteristic impedance | Branch-specific |
| | $C$i | Compliance | Arterial elasticity | Inactive (dP/dt≈0) |
| **CoA segment** | $L$ CoA | Inertance | Blood inertia | Negligible at steady state |
| **Proximal aorta** | $Q$ mv | Valve outflow | LV systolic ejection | Inlet flow source |
| | $R$ao | Ascending aortic resistance | Proximal aortic impedance | Geometry-related |
| | $R_{prox}$ | Proximal lumped resistance | Unresolved viscous losses | Stabilizes inlet pressure |
| | $C_{prox}$ | Proximal compliance | Elastic storage of AAO | Retained for completeness |
| | $C_{aout}$ | Distal compliance | Descending aortic buffering | Degenerates at peak systole |

At the peak-systolic steady-state operating point (dP/dt≈0), all three-element Windkessel (3WK) outlets degenerate to purely resistive loads. Compliance elements are retained for physiological interpretability and consistency with the full 3WK formulation but do not contribute to the governing equations. BP = blood pressure; PSPD = peak systolic pressure difference; PW = pulsed-wave Doppler; CoA = coarctation of the aorta.

## Figure legends

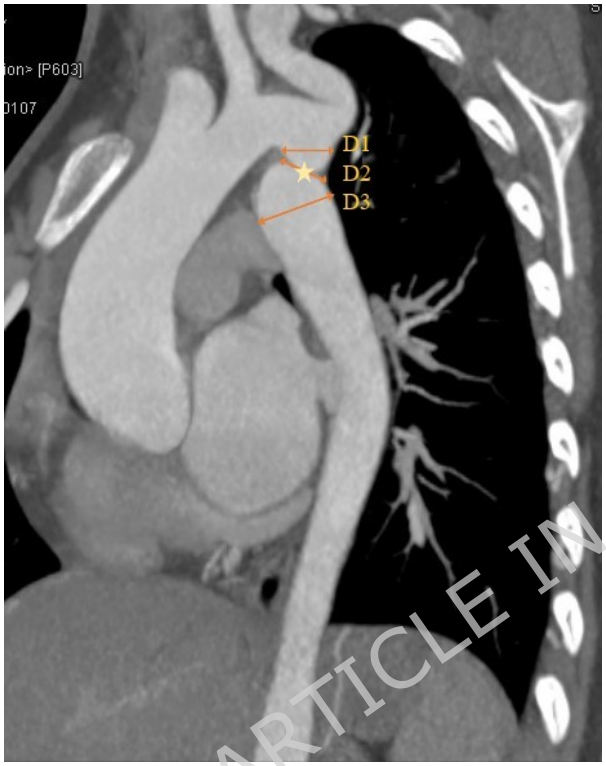




**Figure 1** A sagittal maximum-intensity projection image from MDCTA scan showing the measurement of the CoA. D1: maximum diameters of the posterior transverse arch; D2□maximum diameters of isthmus; D3: distal coarcted descending aorta. ★: CoA length

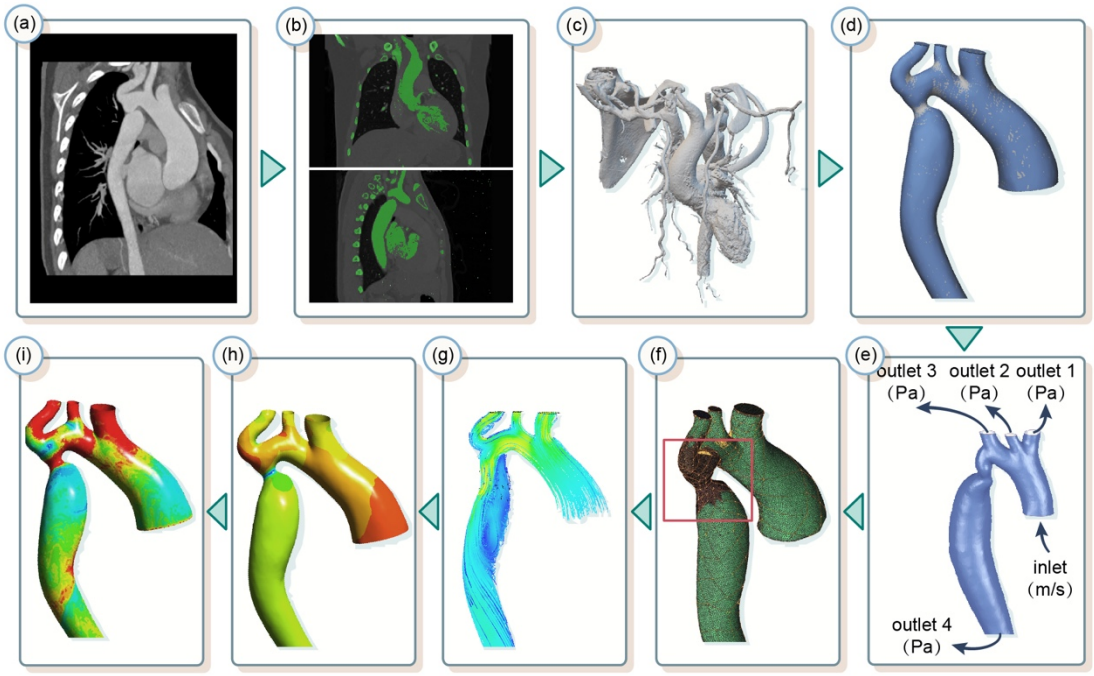


**Figure 2** Framework of the MDCTA-based CFD method. MDCTA data were loaded to the software for geometry reconstruction (ab), segmentation (c) and optimization (d). (e) The 3D anatomy with the inlets and outlets was generated and boundary conditions were defined. (f) Mesh generations were based on the 3D geometric models. (c) CFD simulations were executed for each patient case from MDCTA data to provide information of hemodynamics including velocity field (g), pressure (h) and peak systolic wall shear stress distribution (i) by placing planes in locations of interests.

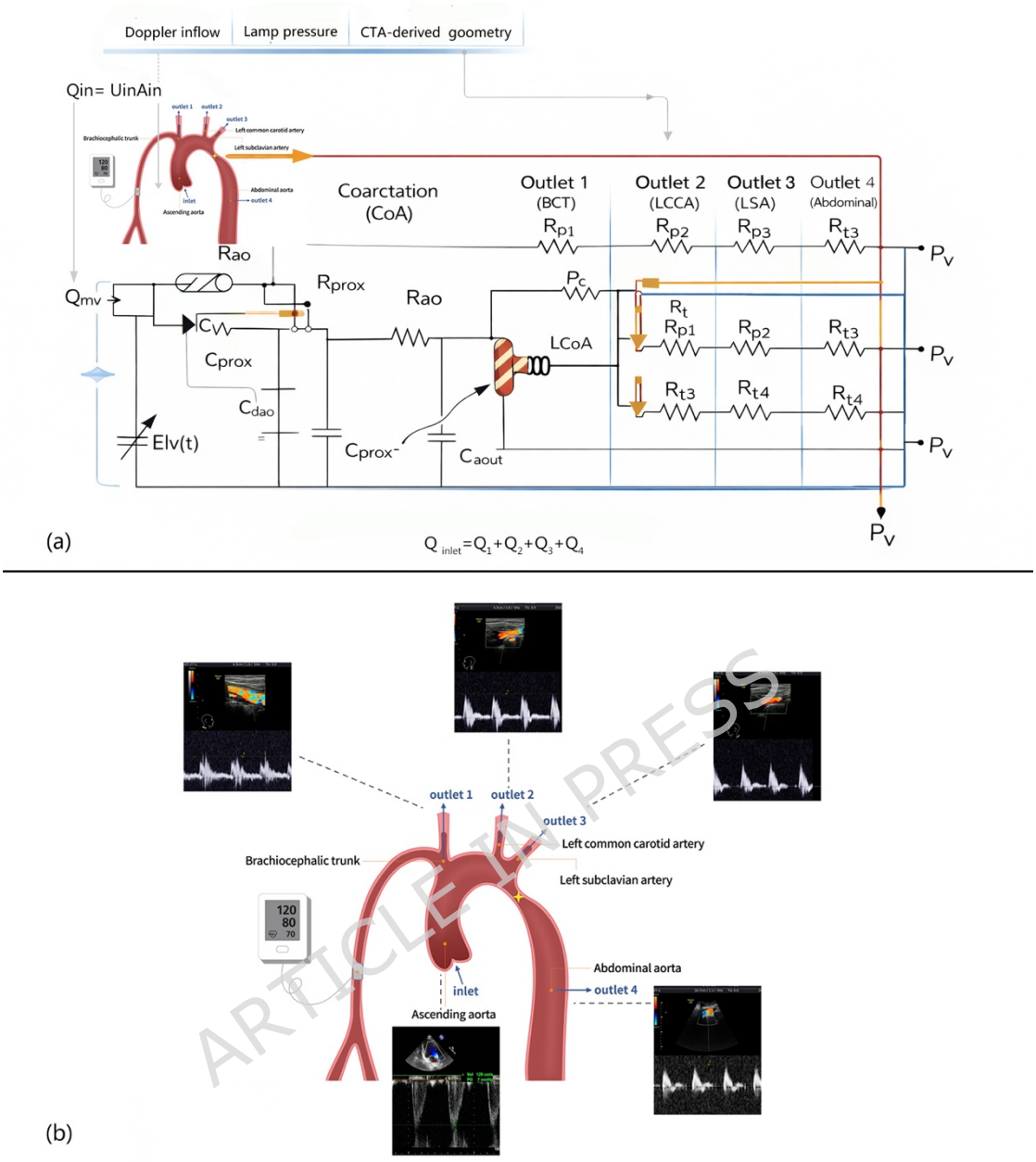


**Figure 3** (a) Schematic diagram of the lumped parameter model. At the peak-systolic steady-state operating point (dP/dt ≈ 0), all three-element Windkessel (3WK) outlets degenerate to purely resistive loads. (b) This is a patient-specific model based on upper BP and Doppler, outlet (1, 2, 3, 4) pressures were defined at peak systole using cuff blood pressure measurements combined with Doppler-derived peak systolic pressure differences (PSPD): Inlet (AAO): $P_{inlet}$ = $P_{RU}$ +PSPD$_{BCT}$ ($P_{outlet1}$) + PSPD$_{AAO}$; Outlet pressures were prescribed as: $P_{out1}$ = $P_{RU}$ +PSPD$_{BCT}$; $P_{out2}$ = $P_{out1}$–PSPD$_{LCCA}$; $P_{out3}$ = $P_{LU}$ + PSPD$_{LSA}$; $P_{out4}$ = $P_{LL}$ + PSPD$_{AbAO}$.( 1mmHg=133.3Pa) BCT: Brachiocephalic trunk; LCCA: Left common carotid artery; LSA: Left subclavian artery; AbAO: Abdominal aorta.

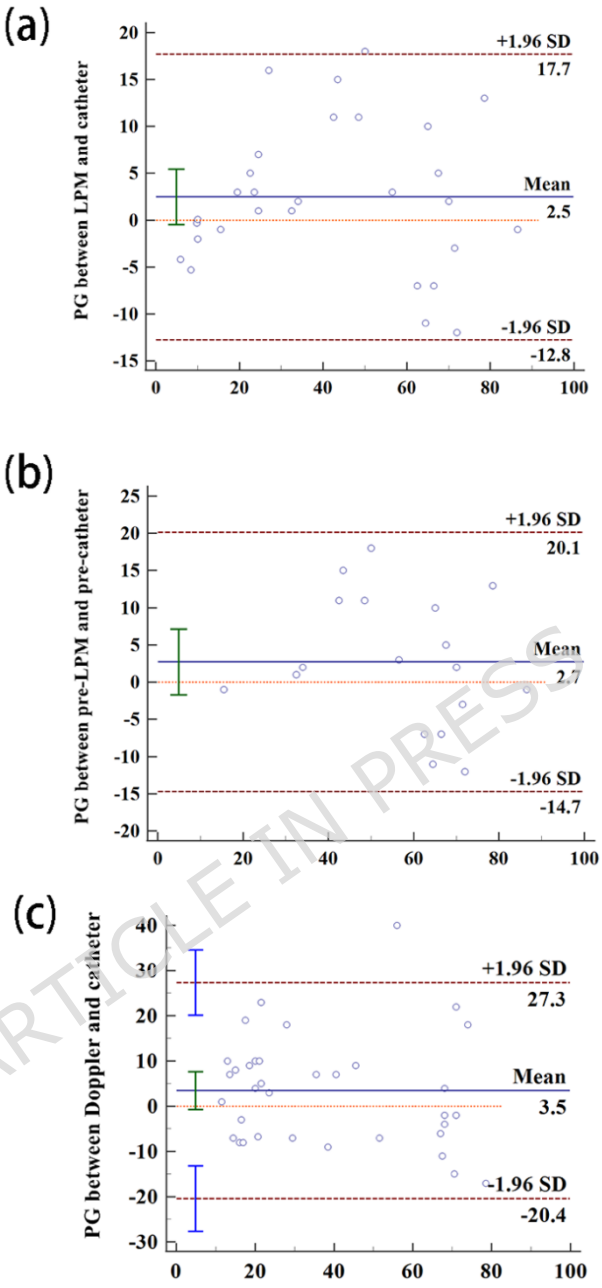


**Figure 4** Bland-Altman plots demonstrating the agreement between pressure gradients (mmHg) measured by CFD stimulation and cardiac catheterization (a and b), as well as between doppler and catheter (c). a and c: pre- and post-treatment. b: pre-treatment.

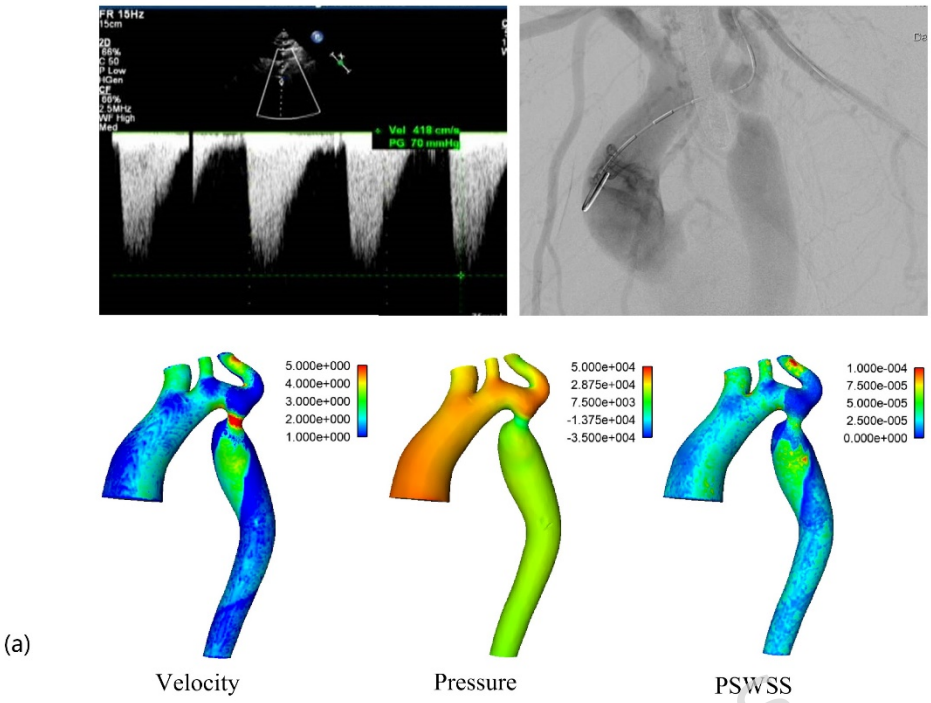


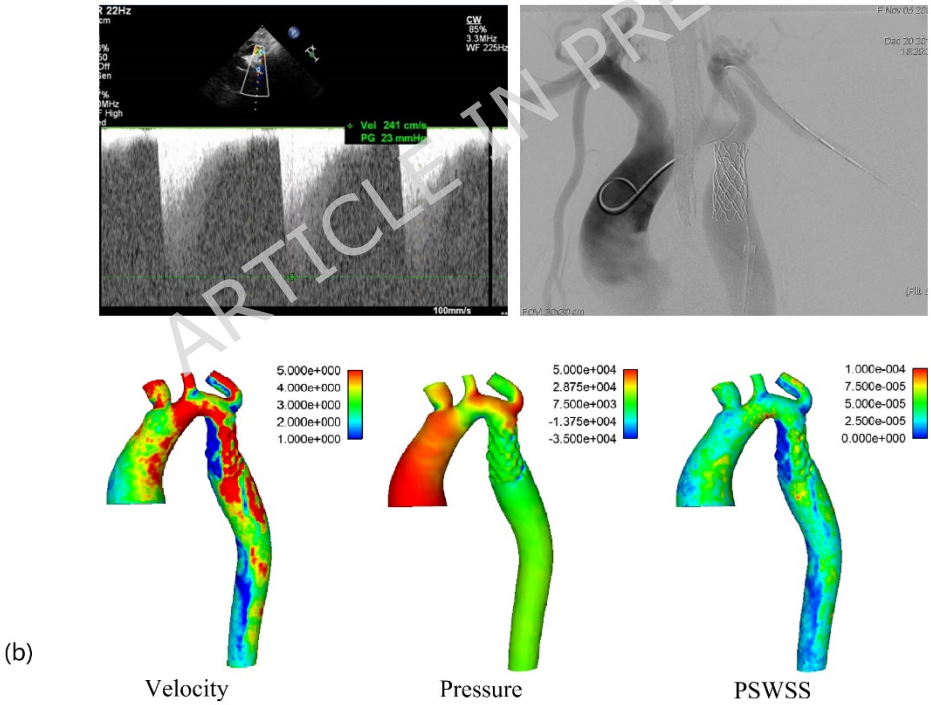




**Figure 5 Pre- and post-intervention hemodynamic alterations in patient in patient #1.** Velocity, Wall pressure (gauge), PSWSS distributions at peak systole are shown with a unified color scale for pre- and post-intervention comparisons. Wall pressure is reported relative to the reference pressure. (a) Pre-intervention, PGs of 26, 35 and 33 mmHg across the coarctation site were measured by Doppler, CFD and catheter respectively. Mean relative error (MRE) of 21%

was reported from Doppler estimates against catheter measurement and MRE of 6% for simulated PG against catheter measurement. (b) Post-intervention, the PGs across the stent decreased to 16, 13.3 and 10 mmHg, as measured by Doppler, CFD and catheter respectively, with MRE of 60% from Doppler against catheter and MRE of 12% from CFD against catheter. (1mmHg=133.3Pa).

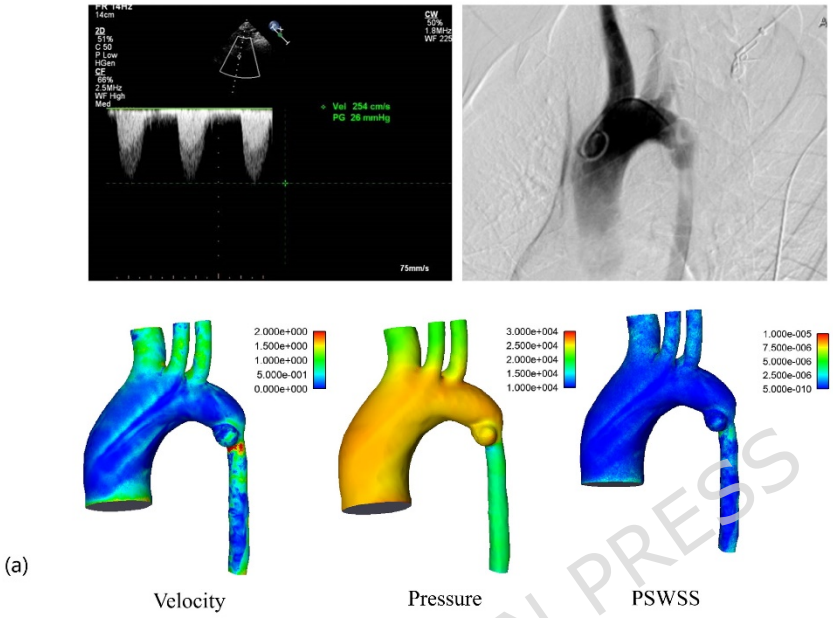


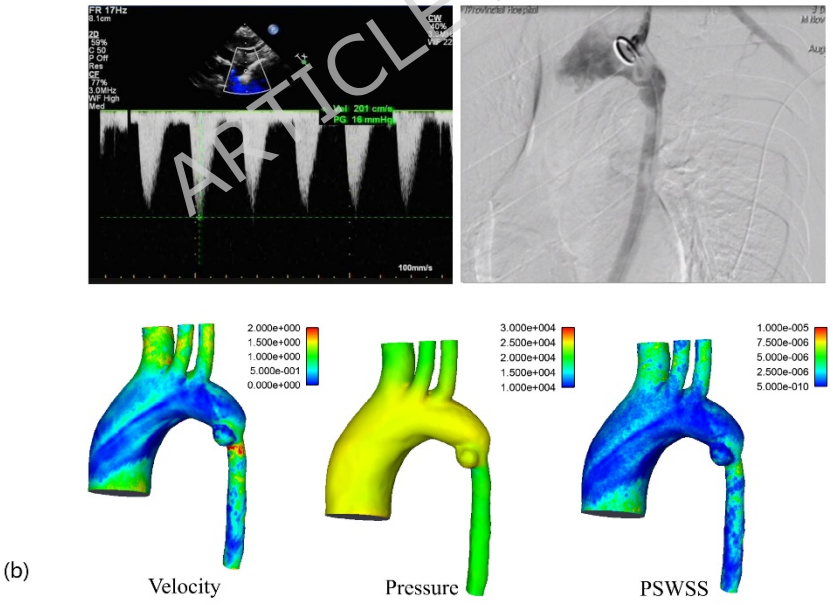




**Figure 6 pre- and post-intervention hemodynamic alterations in patient in patient #2**. (a) Pre-intervention, PGs of 70, 86 and 87 mmHg across the coarctation site were measured by Doppler, CFD and catheter respectively. MRE of 19% was reported from Doppler estimates against catheter measurement and MRE of 1.1% for

simulated PG against catheter measurement. Peak velocity of 4.65m/s was observed at the coarctation, with helical flow at the distal wall of descending aorta. Elevated peak-systolic wall pressure (static/gauge) was observed at the lateral walls of the ascending aortic root and the supra-aortic branches. The maximum PSWSS of 100 Pa was localized at the supra-aortic branches. (b) Post-intervention, the PGs decreased to 23, 25 and 22 mmHg by Doppler, CFD and catheter respectively, with MRE of 4.5% from Doppler against catheter and MRE of 13.6% from CFD against catheter. The peak flow velocity reduced to 2.5m/s, with the helical flow reduced. Peak systolic pressure was noted at the ostia of supra aortic branches, with the range also narrowed down. And the maximum PSWSS reduced to 50.6 Pa, with a distribution of lateral wall of the deployed stent and ostium of the left subclavian artery. (1mmHg=133.3Pa).

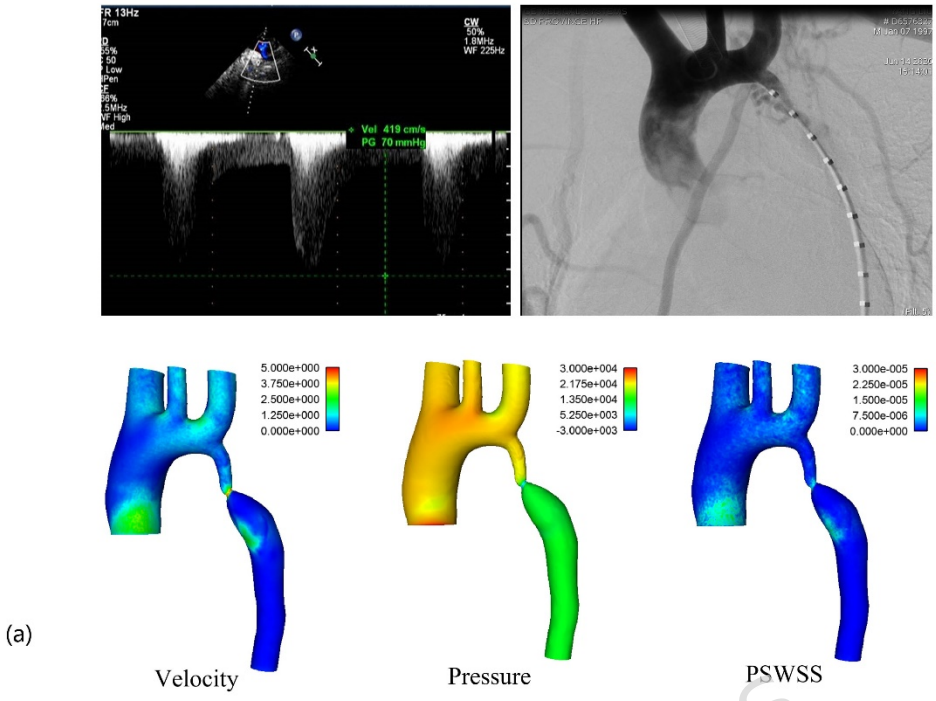


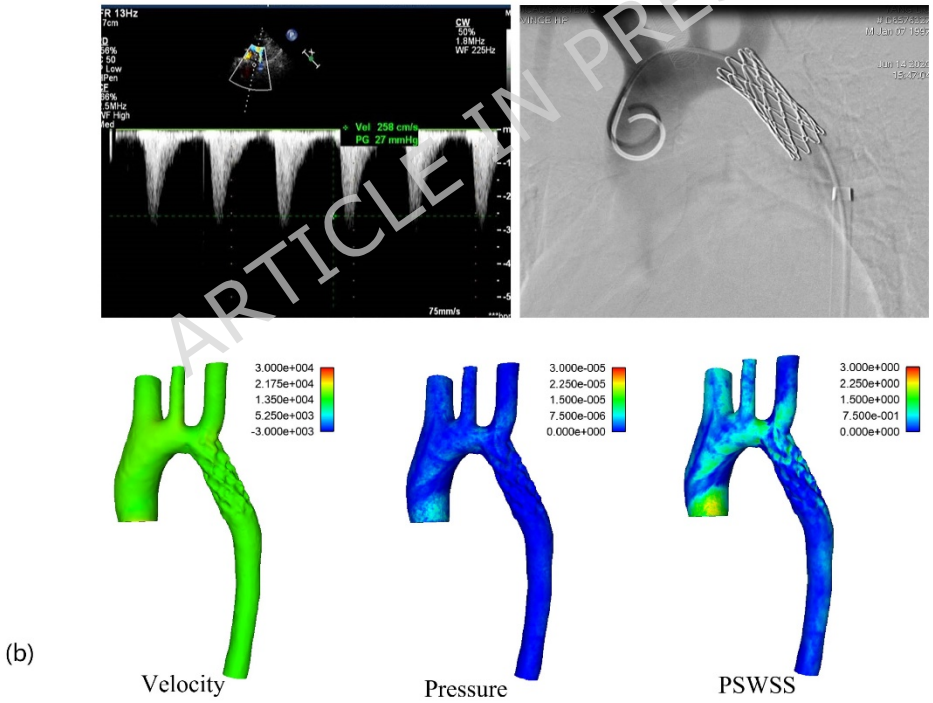




**Figure 7 Pre- and post-intervention hemodynamic alterations in patient in patient #5**. (a) Before the intervention, the maximum flow velocity of 4.63m/s was simulated at the coarctation and formed helical flow after the coarctation site. Peak-systolic wall pressure (static/gauge) of 196 mmHg was detected at the lateral wall of the coarctation site. And PSWSS of 197 Pa was distributed at the connection between coarctation and descending aorta. (for

visualization; trans-coarctation PG is reported separately based on the Bernoulli equation). (b) After the intervention, the maximum velocity was reduced to 3.28m/s and distributed at ascending aorta. Peak-systolic wall pressure (static/gauge) of 15.8 mmHg was induced at the root of the ascending aorta. And reduction of PSWSS of 109Pa was found at the lateral wall of the root of the ascending aorta. (1mmHg=133.3Pa).

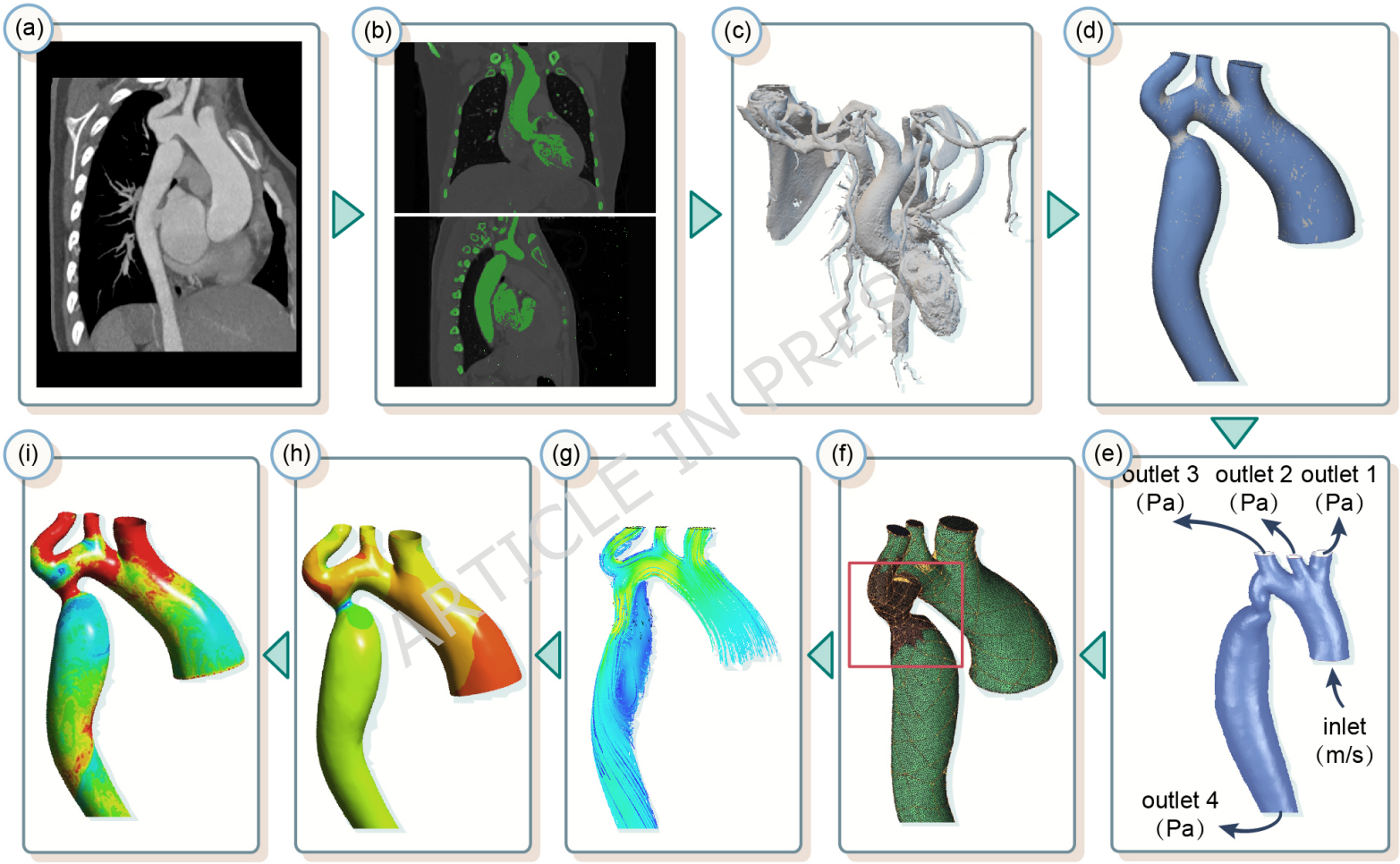

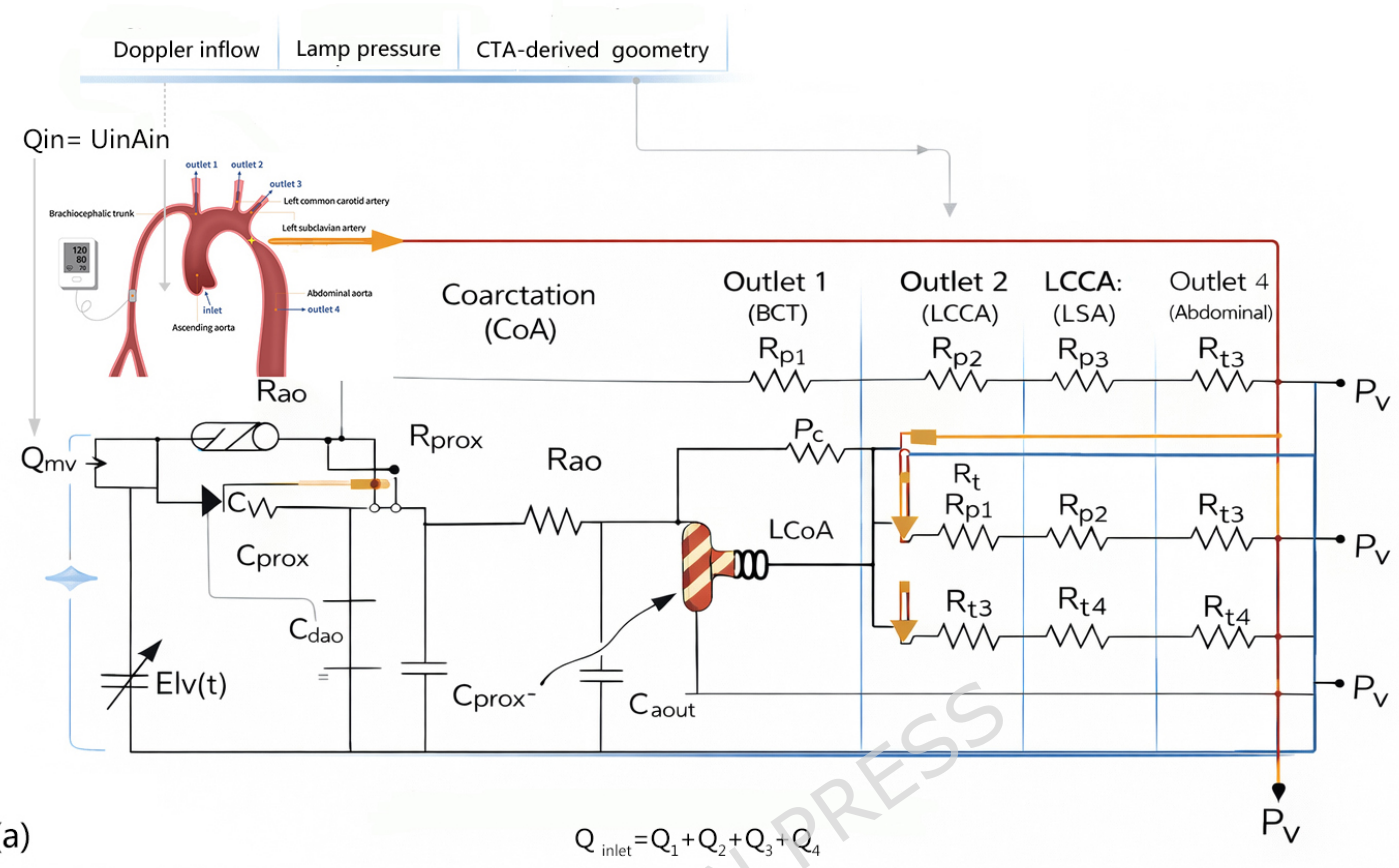


(a)

$$Q_{inlet} = Q_1 + Q_2 + Q_3 + Q_4$$

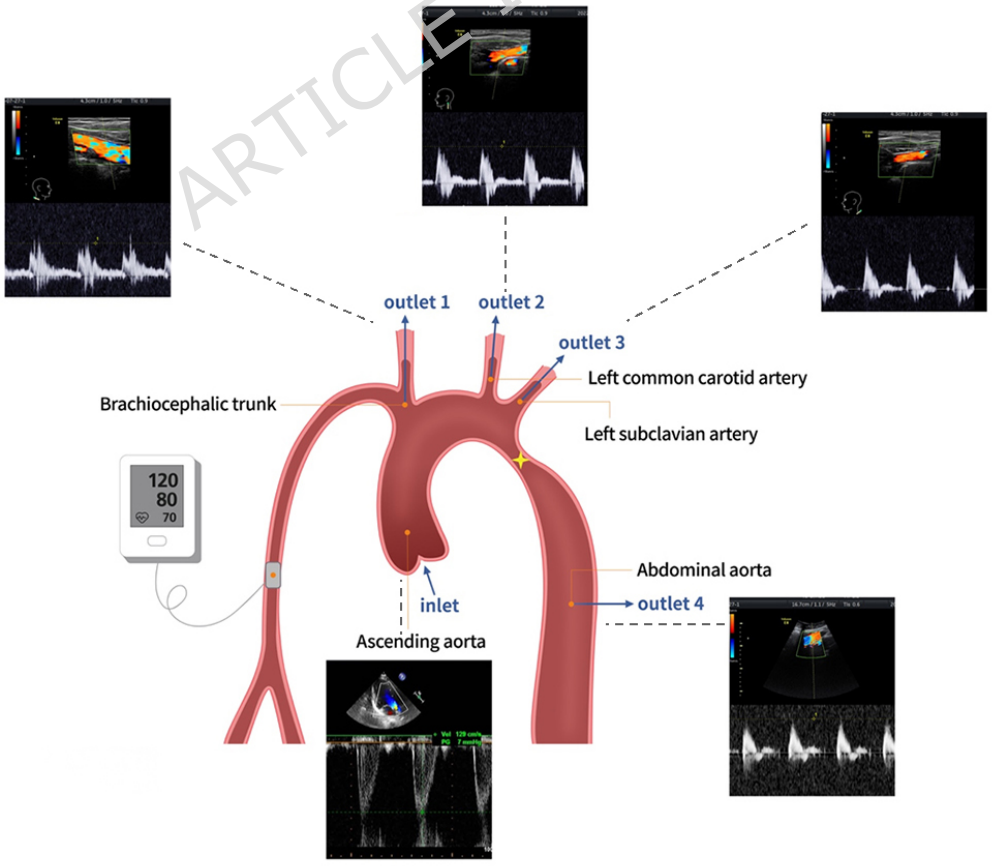


(b)

(a)

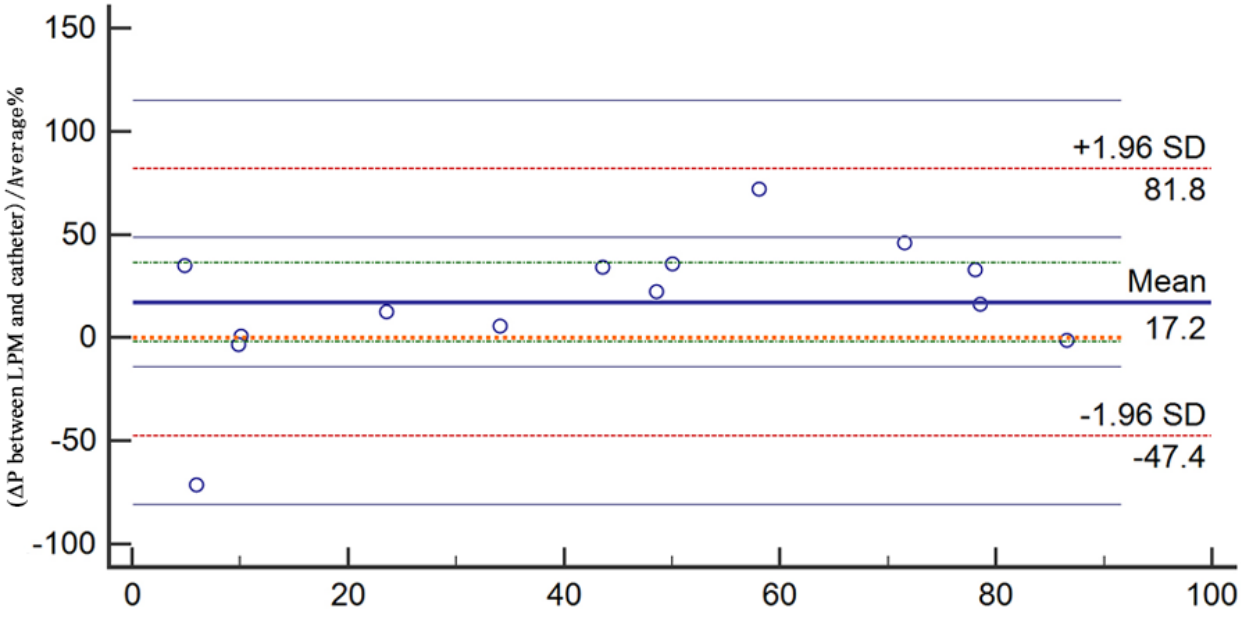


(b)

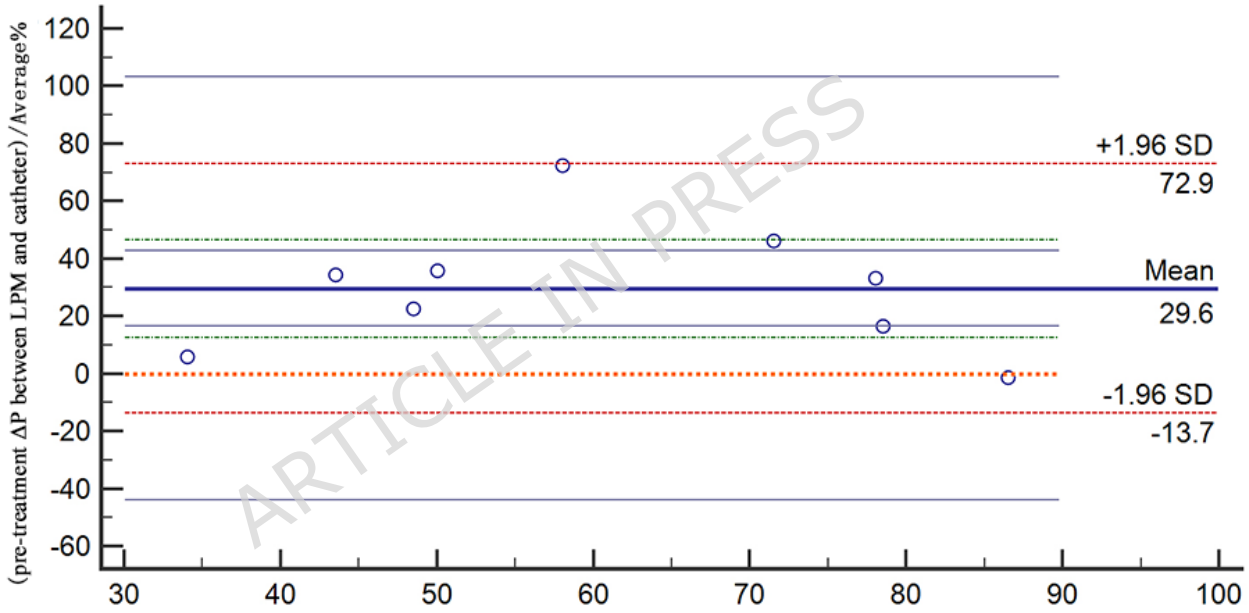




(c)

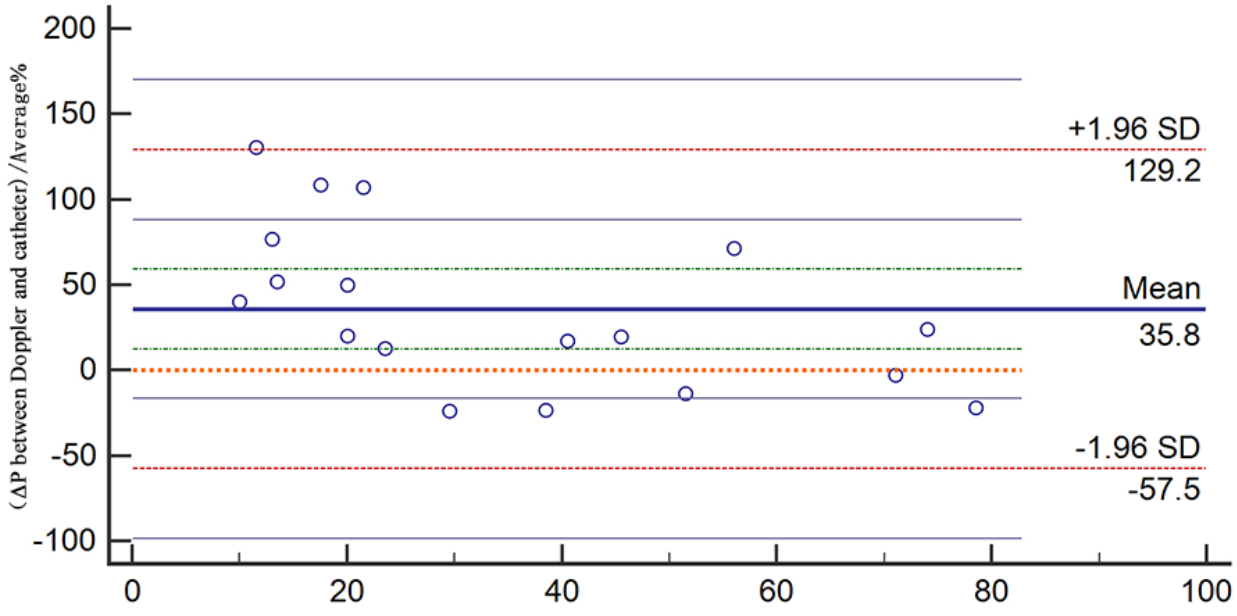

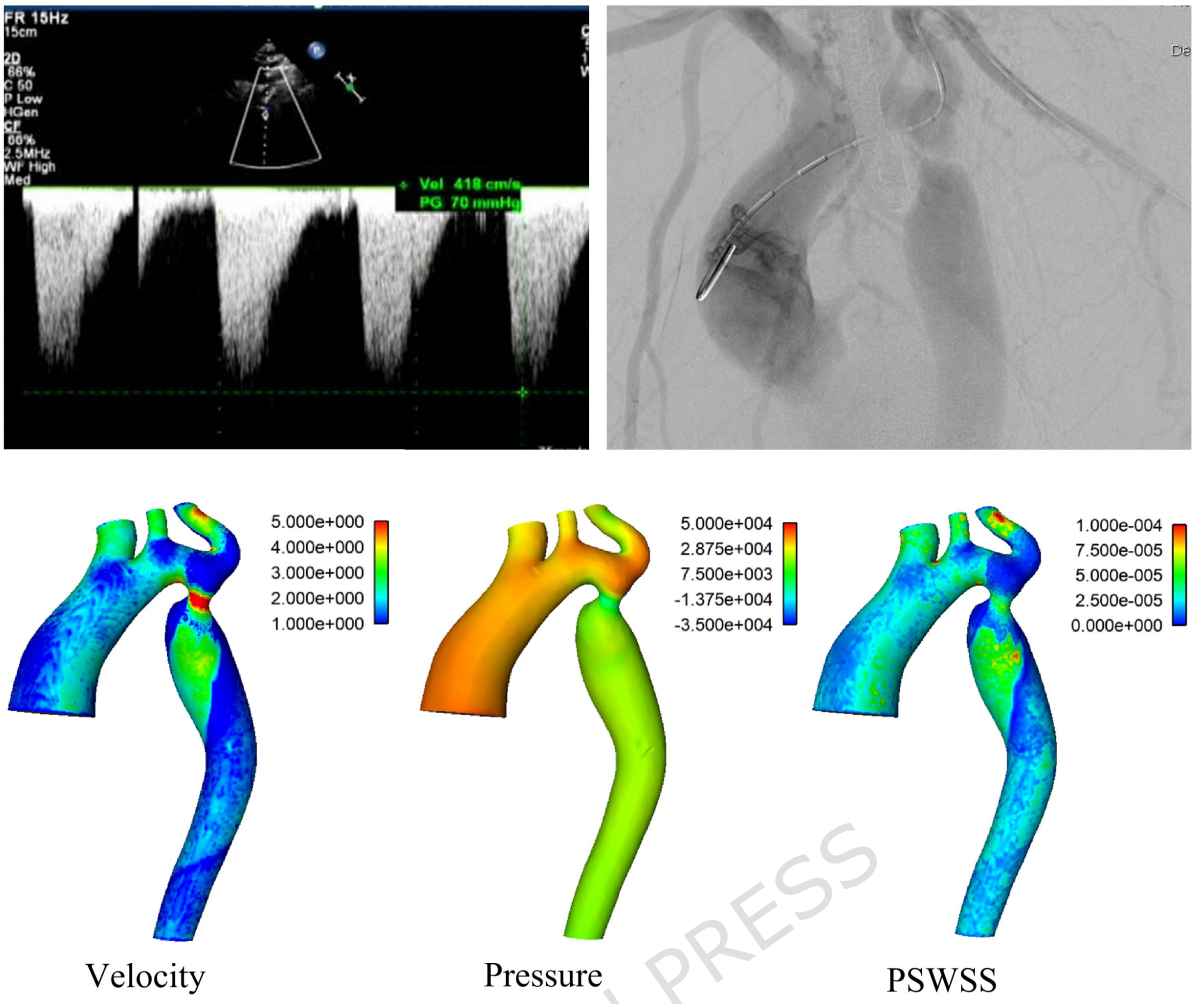


(a)

Velocity Pressure PSWSS

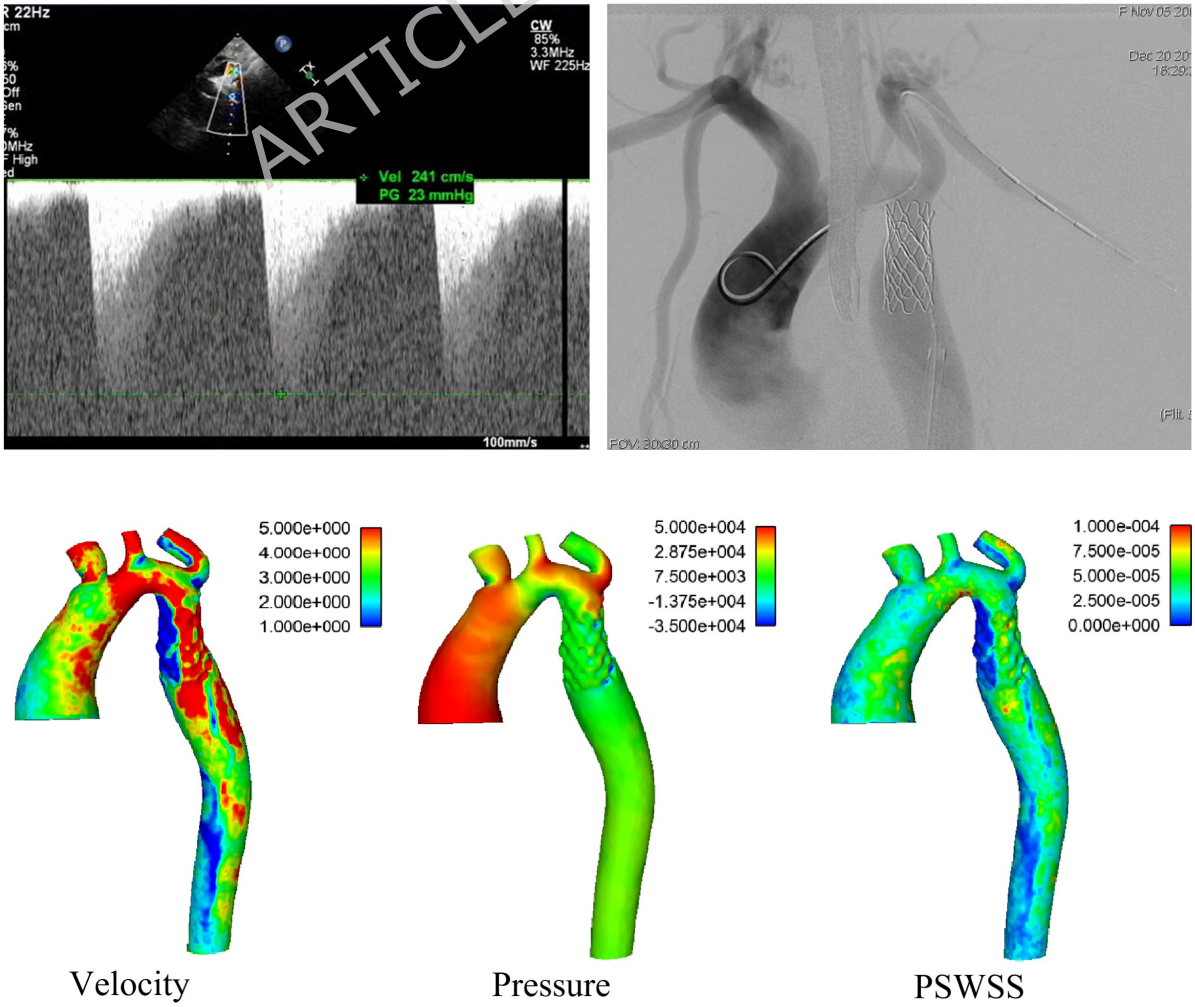


(b)

Velocity Pressure PSWSS

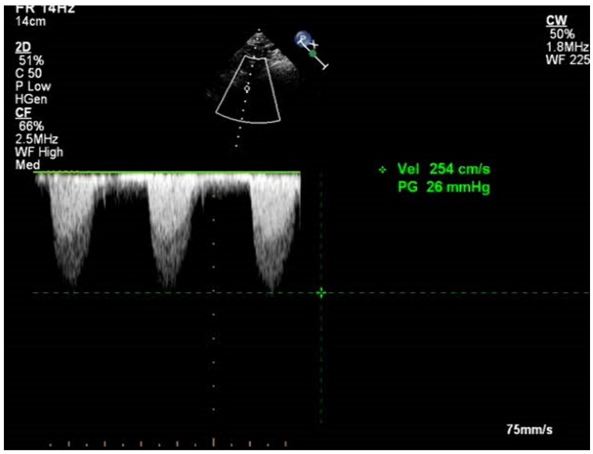


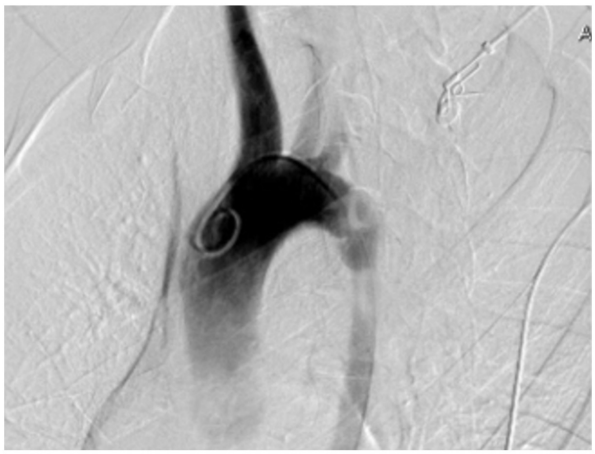

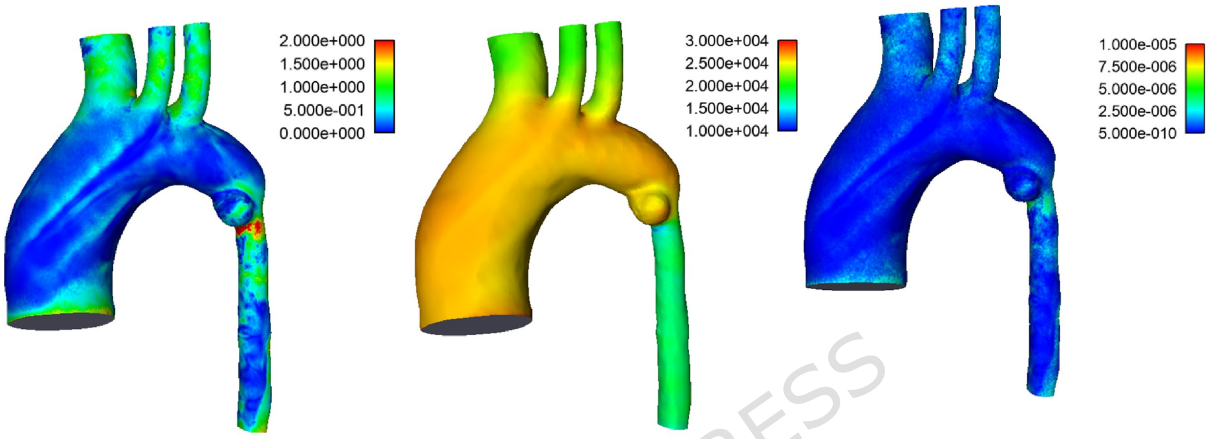


(a)

Velocity Pressure PSWSS



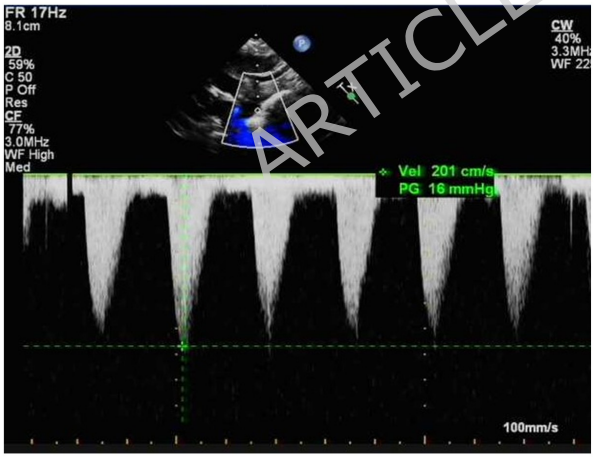


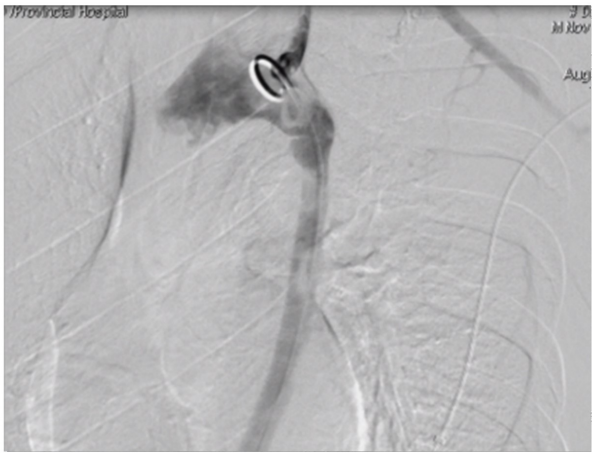

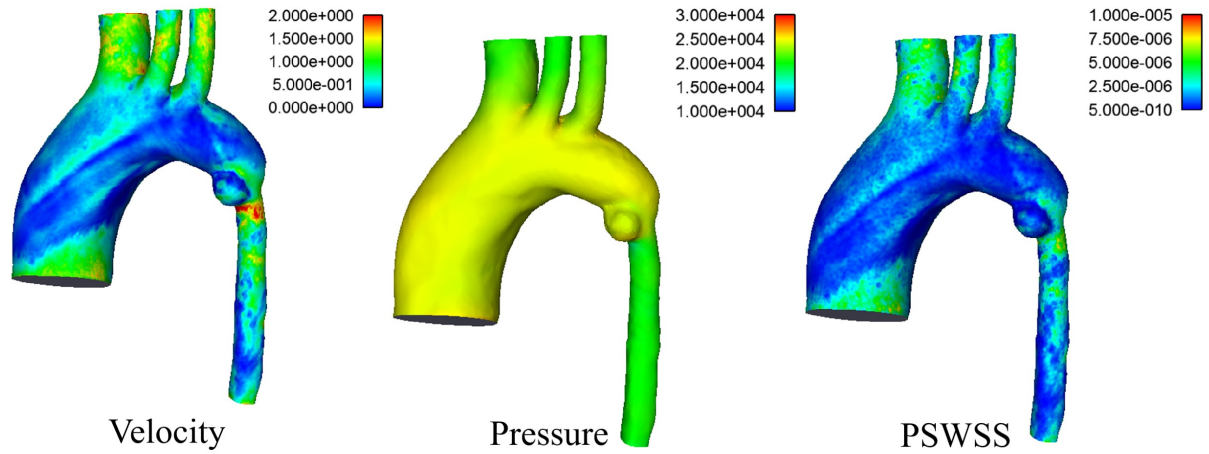


(b)

Velocity Pressure PSWSS

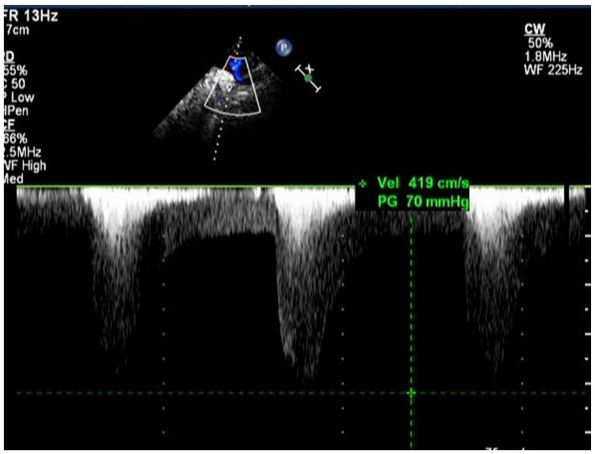


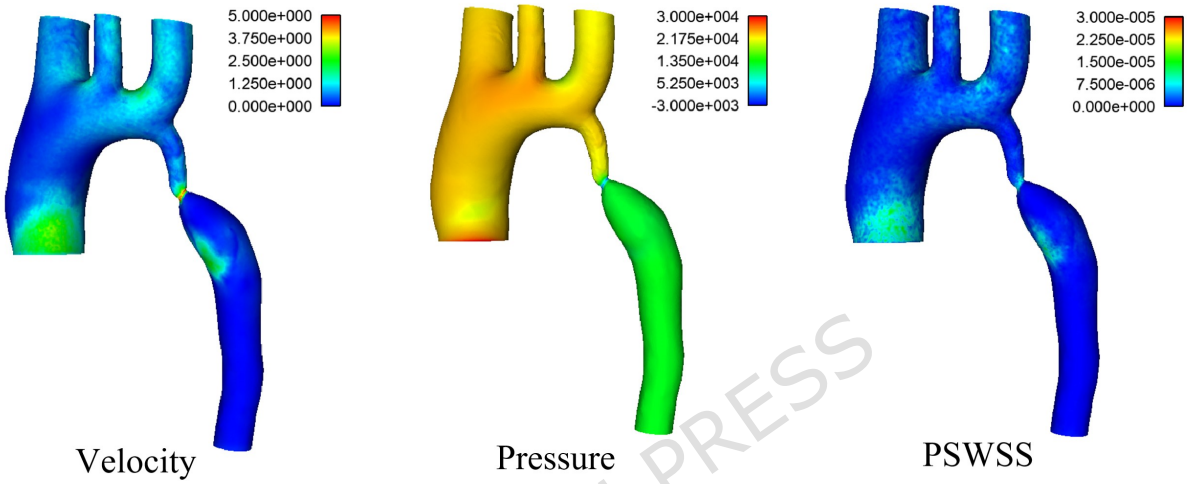


(a)

Velocity Pressure PSWSS



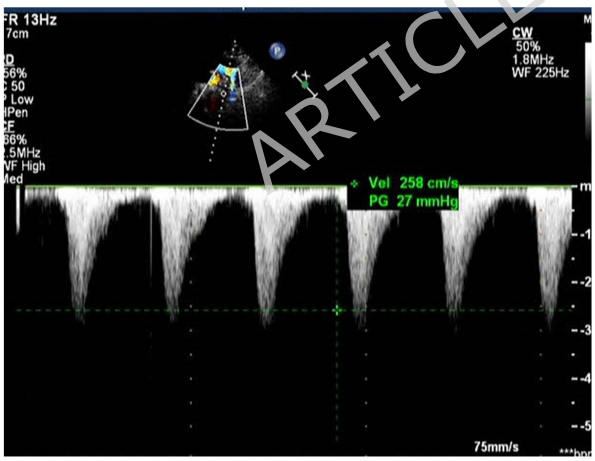


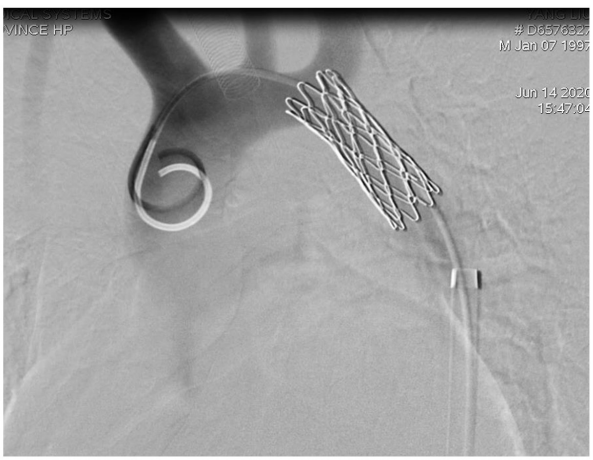

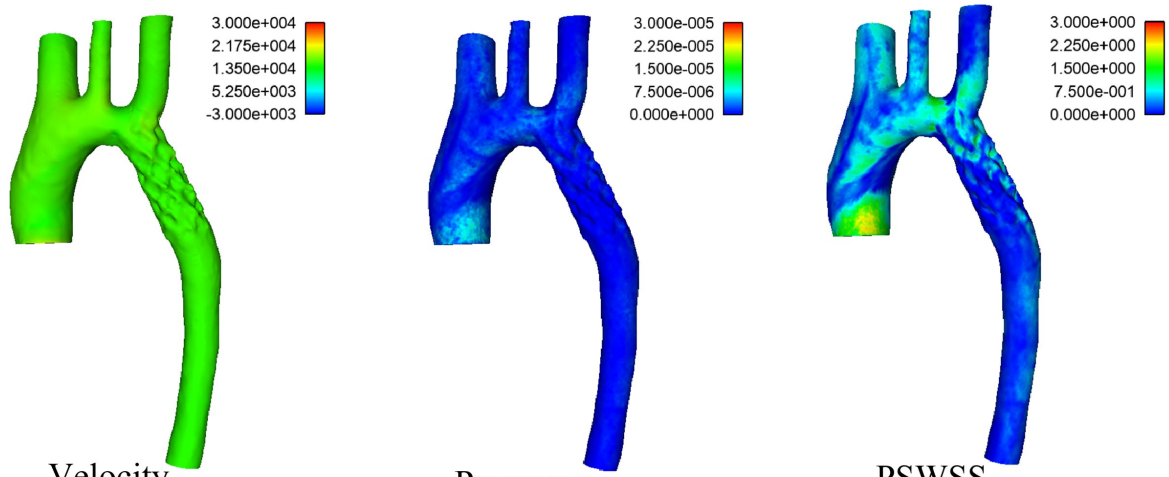


(b)

Velocity Pressure PSWSS

**Table 1**
**Patient characteristics and pre-interventional morphologic parameters of the aortic arch from MDCTA.**

| Cases | Sex | Age (years) | D1 (cm) | D2 (cm) | D3 (cm) | CoA length (cm) | Interventional treatments |
|---|---|---|---|---|---|---|---|
| No.1 | Female | 14 | 3.5×3.2 | 1.3×1.2 | 3.0×2.6 | 0.6 | BIB catheter dilation+ stent |
| No.2 | Male | 16 | 3.7 | 0.9 | 1.0 | 3.6 | Balloon dilation |
| No.3 | Male | 6 | 1.21 | 1.0×0.8 | 2.1×1.9 | 2.25 | Balloon dilation |
| No.4 | Female | 22 | 1.5 | 0.6×0.5 | 3.0 | 4 | BIB catheter dilation+ CP stent |
| No.5 | Male | 16 | 1.3 | 0.19 | 1.4 | 3.5 | BIB balloon dilation+ CP stent |
| No.6 | Female | 29 | 3.2×3.2 | 0.61 | 0.95×0.95 | 3.77 | CP stent |
| No.7 | Male | 32 | 1.7 | 0.7 | 4.2 | 2.1 | BIB catheter dilation+ stent |
| No.8 | Female | 20 | 1.6 | 0.6 | 3.3 | 4.0 | BIB catheter dilation+ stent |
| No.9 | Male | 40 | 3.1×3.0 | 0.8×0.6 | 1.6×1.7 | 3.0 | CP stent |
| No.10 | Female | 13 | 2.0 | 0.56 | 2.9 | 2.3 | Balloon dilation |
| No.11 | Male | 16 | 3.2 | 0.43 | 3.37 | 1.90 | BIB catheter dilation+ stent |
| No.12 | Male | 7 | 1.34 | 0.65 | 2.1 | 1.89 | Balloon dilation |
| No.13 | Male | 49 | 4.1 | 1.23 | 4.32 | 2.31 | BIB catheter dilation+ stent |
| No.14 | Male | 23 | 2.90 | 1.23 | 3.23 | 1.67 | CP stent |
| No.15 | Male | 9 | 2.45 | 0.99 | 2.95×3.0 | 2.1 | Balloon dilation |
| No.16 | Female | 19 | 3.11 | 1.45 | 3.12 | 1.33 | CP stent |
| No.17 | Male | 23 | 2.98 | 1.09 | 3.78 | 2.11 | CP stent |
| No.18 | Female | 19 | 3.12 | 1.33 | 2.76 | 1.67 | BIB catheter dilation+ stent |

D1: maximum diameters of the posterior transverse arch; D2 □ maximum diameters of isthmus; D3: distal coarcted descending aorta; BIB: balloon in balloon; CP: cheatham-platinum

**Table 2**

**Mesh details of all Patient.**

| Cases | | Number of Elements | |
|---|---|---|---|
| | | Pre-intervention | Post-intervention |
| **No.1** | | 2720270 | 3450987 |
| **No.2** | | 1715637 | 2219870 |
| **No.3** | | 2761918 | 3005065 |
| **No.4** | | 5271231 | - |
| **No. 5** | Coarse | 1819196 | 5992477 |
| | Fine | 5302881 | |
| | Refined | 7999464 | |
| **No.6** | | 3378190 | 4267781 |
| **No.7** | | 2097610 | - |
| **No.8** | | 3901456 | 4002398 |
| **No.9** | | 4923709 | - |
| **No.10** | | 2793026 | 3317011 |
| **No.11** | | 6510455 | 6901986 |
| **No.12** | | 5017621 | - |
| **No.13** | | 4903657 | - |
| **No.14** | | 3996708 | 4602361 |
| **No.15** | | 2904489 | - |
| **No.16** | | 2290643 | 3872460 |
| **No.17** | | 3804383 | - |
| **No.18** | | 5610934 | 6346898 |

-: Patient lost to follow-up.

**Table 3**
**Inter-and intra-observer agreement for the morphological values.**

| Parameters | Inter-observer | | Intra-observer | |
|---|---|---|---|---|
| | ICC | 95%CI | ICC | 95%CI |

| | | | | |
|---|---|---|---|---|
| D1 | 0.969 | (0.871-0.993) | 0.975 | (0.967-0.986) |
| D2 | 0.831 | (0.419-0.959) | 0.965 | (0.917-0.980) |
| D3 | 0.982 | (0.923-0.996) | 0.975 | (0.977-0.992) |
| CoA length | 0.991 | (0.959-0.998) | 0.971 | (0.958-0.989) |

D1: maximum diameters of the posterior transverse arch; D2：maximum diameters of isthmus; D3: distal coarcted descending aorta; CI: confidence interval.

**Table 4**
**Pre- and post-interventional biochemical and physiological indexes.**

| | | Pre-intervention | Post-intervention | P value |
|---|---|---|---|---|
| BP (mmHg) | Left upper arm | 162.6±17.9 | 126.2±13.1 | 0.000 |
| | Right upper arm | 165.8±22.8 | 127.1±12.2 | 0.000 |
| | Left lower limb | 107.5±17.3 | 114.2±15.3 | 0.109 |
| | Right lower limb | 114.7±15.3 | 115.1±15.1 | 0.945 |
| BPD (mmHg) | Left AABPD | 55.1±15.3 | 12.0±9.68 | 0.000 |
| | Right AABPD | 51.1±21.5 | 12.0±11.1 | 0.000 |
| | IASBPD | 3.2±10.8 | 0.88±4.98 | 0.486 |
| LVEF (%) | | 62.1±1.6 | 60.9±1.4 | 0.179 |
| Serum creatinine (μmol/L) | | 60.7±14.5 | 56.9±15.6 | 0.007 |
| eGFR (ml/(min·1.73m$^2$) | | 123.7±25.1 | 133.2±26.5 | 0.041 |
| Blood urea nitrogen (mmol/L) | | 5.11±0.77 | 4.58±1.15 | 0.060 |

AABPD: arm-ankle blood pressure difference; IASBPD: inter-arm blood pressure difference

**Table 5. Summarized cardiovascular parameters used in the LPM coupled with CFD**

| Category | Symbol | Definition / Formula | Physiological meaning | Role in this study |
|---|---|---|---|---|
| **Inlet flow** | $Q_{in}$ | $Q_{in} = U_{in} A_{in}$ | Ascending aortic volumetric inflow at peak systole | CFD inlet flow boundary |
| | $U_{in}$ | Area-averaged inlet velocity | Mean systolic inflow velocity | Derived from Doppler with correction |
| | $A_{in}$ | CTA-derived inlet area | Cross-sectional area of ascending aorta | Geometry-based |
| **Pressures** | $P_{in}$ | | Peak systolic ascending aortic pressure | Constructed from cuff BP + PSPD |
| | $P_{out,\ i}$ | Prescribed | Outlet peak systolic pressure | Pressure-outlet BC |
| | $P_v$ | Reference pressure | Venous reference pressure | Common downstream reference |
| | $Q_i$ | $\int_{A_i} u \cdot n \cdot dA$ | Branch flow rate | CFD-computed |

| | | | | |
|---|---|---|---|---|
| **Flow conservation** | — | Qin=Q1+Q2+Q3+Q4 | Mass conservation | Closed-loop consistency |
| **Outlet load (3WK)** | $R$ t, i | (ΔP i=Rt,iQ_i) | Effective outlet resistance | Active load at peak systole |
| | $R$ p, i | Proximal resistance | Characteristic impedance | Branch-specific |
| | $C$i | Compliance | Arterial elasticity | Inactive (dP/dt≈0) |
| **CoA segment** | $L$ CoA | Inertance | Blood inertia | Negligible at steady state |
| **Proximal aorta** | $Q$ mv | Valve outflow | LV systolic ejection | Inlet flow source |
| | $R$ao | Ascending aortic resistance | Proximal aortic impedance | Geometry-related |
| | $R_{\text{prox}}$ | Proximal lumped resistance | Unresolved viscous losses | Stabilizes inlet pressure |
| | $C_{\text{prox}}$ | Proximal compliance | Elastic storage of AAO | Retained for completeness |
| | $C_{\text{aout}}$ | Distal compliance | Descending aortic buffering | Degenerates at peak systole |

At the peak-systolic steady-state operating point (dP/dt≈0), all three-element Windkessel (3WK) outlets degenerate to purely resistive loads. Compliance elements are retained for physiological interpretability and consistency with the full 3WK formulation but do not contribute to the governing equations. BP = blood pressure; PSPD = peak systolic pressure difference; PW = pulsed-wave Doppler; CoA = coarctation of the aorta.